University of Rhode Island

DigitalCommons@URI

2020

SUBSEAFLOOR POREWATER PALEOSALINITY AND NITROGEN ISOTOPES

Kira Louise Homola
University of Rhode Island, khomola@uri.edu

Follow this and additional works at: https://digitalcommons.uri.edu/oa_diss

SUBSEAFLOOR POREWATER PALEOSALINITY AND NITROGEN ISOTOPES

BY

KIRA LOUISE HOMOLA

A DISSERTATION SUBMITTED IN PARTIAL FULFILLMENT OF THE

REQUIREMENTS FOR THE DEGREE OF

DOCTOR OF PHILOSOPHY

IN

OCEANOGRAPHY

UNIVERSITY OF RHODE ISLAND

2020

DOCTOR OF PHILOSOPHY DISSERTATION

OF

KIRA LOUISE HOMOLA

APPROVED:

Dissertation Committee:

Major Professor Arthur Spivack

 Rebecca Robinson

 Simon Engelhart

Dean of the Graduate School Nasser H. Zawia

UNIVERSITY OF RHODE ISLAND

2020

ABSTRACT

Sedimentary porewater chemical and isotopic profiles contain complex records of past bottom water composition which are overprinted by in situ biotic and abiotic reactions. We developed a density-based method to determined relic deep water salinities and applied it to map global scale water mass properties and distributions in the deep northwest Atlantic at four previously unsampled sites. Paleosalinities determined by density have higher precision and accuracy than previously published results and confirm the northward expansion of southern deep water and a reversal in the Atlantic's bottom water meridional salinity gradient during the Last Glacial Maximum (Chapters 1 & 2).

Nitrogen isotopic composition profiles of deeply buried porewaters are a unique dataset used to distinguish between biotic and abiotic nitrogen reactions under conditions that approach the canonical temperature and pressure limits of life. We attribute observed variations in nitrogen concentrations and isotopic compositions of porewater and sediment to a variety of microbially mediated processes including assimilation, ammonification, sulfate reducing ammonia oxidation, accretion, dissolution, and illitization (Chapter 3).

ACKNOWLEDGMENTS

DEDICATION

       This dissertation is dedicated to my family, friends, and familiars of formidable, feathered, finned, and especially furred persuasions: thank you for your love and inspiration.

<u>PREFACE</u>

This dissertation is written in manuscript format. All three manuscripts are presented in full sequence, excepting references and appendices that can be found at the end. Tables and Figures are numbered sequentially by manuscript (e.g. figure 2.4 is figure 4 in manuscript 2).

The first manuscript, *High Precision Paleosalinity Determined from Measured Porewater Density*, has been submitted for publication in Marine Chemistry.

The second manuscript, *Deep North Atlantic Last Glacial Maximum Salinity Reconstruction*, is prepared for publication in Paleoceanography.

The third manuscript, *Nitrogen Abundance and Isotopic Composition of Subducting Deep Subseafloor Sediment and Porewater, Site IODP-C0023*, is prepared for publication in Geochemistry, Geophysics, Geosystems.

TABLE OF CONTENTS

Nitrogen Abundance and Isotopic Composition of Subducting Deep Subseafloor

Sediment and Porewater at Site IODP-C0023

LIST OF TABLES

LIST OF FIGURES

MANUSCRIPT 1

High Precision Paleosalinity

Determination from Measured Porewater Density

by

Kira L. Homola[1], Arthur J. Spivack[1], Richard W. Murray[2]

Submitted to *Marine Chemistry*

---

[1]University of Rhode Island Graduate School of Oceanography
[2]Woods Hole Oceanographic Institution

Abstract

We have developed a density-based method for determining porewater salinity that can be performed shipboard on small volume samples with greater efficiency and precision than the currently available shore-based chloride titration technique. This approach is based on a recently developed water column method that determines salinity at the precision of a conductivity measurement through density measurements and the seawater thermodynamic equation of state. Diagenesis causes deviations in porewater composition from standard seawater values, affecting the density salinity relationship, that we correct for through precise measurements of each ion's concentration before converting measured density to chloride concentration. We account for the diffusive change in porewater chloride that occurs over time independent of diagenesis by optimizing diffusion modeled, sea-level determined bottom water chloride as a function of time to measured modern porewater and converting the best fit to salinity.

We applied our density method to porewater samples extracted from adjacent long cores collected from the deep western North Atlantic, determining Last Glacial Maximum (LGM) bottom water paleosalinity in a region critical to understanding deep water mass distribution. High uncertainty is associated with current LGM bottom water salinity characterizations and their implications for LGM overturning circulation and climate. Density was determined to a precision of 2.3×10^{-6} g/mL, which translates to a relative salinity uncertainty of 0.03% for LGM salinity. We compare the high precision chloride concentration profiles determined using our method to profiles

determined from chloride titrations of parallel samples. Salinity change at our site between the pre-industrial and LGM is 3.07 ± 0.03 % and 3.65 ± 0.06 % when determined from density and 2.96 ± 0.12 % and 1.96 ± 0.21 % when determined from titrated Cl$^-$. This is consistent with nearby deep Atlantic paleosalinity data (Adkins, McIntyre, and Schrag 2002) and global sea-level-change determined salinity change (Clark and Mix 2002). By comparing uncertainties we demonstrate that porewater salinity can be determined to a higher precision and with increased reproducibility through our density protocol compared to titration-determined salinity. Application of our shipboard method at further locations will increase the resolution, precision, and accuracy of available LGM bottom water salinity reconstruction, improving the characterization of glacial deep water masses and overturning circulation.

Introduction and Background

Salinity is used to resolve ocean density structure and the spreading of deep water masses (Munk 1950; Stommel and Arons 1959). Accurate and precise measurement of salinity is critical to evaluating meridional overturning circulation (MOC) and CO_2 transfer between the atmosphere and deep ocean. Characterizing deep water masses in the present and past ocean is vital to constraining glacial-interglacial climate change (Boyle and Keigwin 1982; Schmittner and Galbraith 2008; Toggweiler and Russell 2008). The dynamics and structure of MOC during the most recent glacial maximum (Siegenthaler, Stocker, and Monnin 2005), however, remain difficult to constrain fully with available techniques. During the Last Glacial Maximum (LGM), between 19-26 ka (Clark et al. 2009; Peltier and Fairbanks 2006; Yokoyama et al. 2000), atmospheric CO_2 concentrations were approximately 30% lower than pre-industrial levels (Mix, Bard, and Schneider 2001; Petit et al. 1999), global average sea level was 13 0 meters lower, and average seawater was approximately 3.6% saltier (Clark et al. 2009; Clark and Mix 2002; Peltier and Fairbanks 2006).

Higher bottom water salinity from the LGM is identified directly as a chloride (Cl^-) concentration peak in subseafloor porewaters (Adkins and Schrag 2001; McDuff 1985) influenced by diffusion, advection, and diagenesis. Adkins et al.(2002) interpreted porewater Cl^- and $\delta^{18}O$ using one-dimensional diffusion modeling (e.g. Schrag et al.1992) at several sites in the Atlantic. They achieved average uncertainties for LGM salinity (±0.1 g/kg, 0.3 %) and temperature based on oxygen isotopes (± 0.53 °C) a few orders of magnitude larger than the precision with which we can resolve

these parameters in the modern deep ocean, identifying the largest source of error as the necessary storage of porewater samples between collection and analysis (Adkins and Schrag 2003).

Increasing precision and accuracy in LGM bottom water salinity measurement at more locations will improve the resolution of glacial deep water mass distribution reconstructions, which can be applied to enhance understanding of glacial density-dependent circulation. While high precision water column salinity is routinely determined by conductivity, current porewater salinity measurement techniques rely on Cl^- titration with $AgNO_3$, consuming the sample in the process. Titration precision is limited by how accurately we can measure the mass of solution titrated. Ships are too unsteady to precisely measure mass by weight so mass is quantified by volume onboard. Higher precisions can be achieved on shore by weighing titrated aliquots, but as mentioned above, minimal evaporation introduces artifacts in small samples stored post-expedition (Adkins and Schrag 2003).

To solve this problem, we developed a shipboard porewater density-based measurement method that improves the precision of bottom water salinity reconstruction. Our approach builds upon that of Millero et al. (2009), who determined salinity by measuring seawater density through frequency analysis, achieving a relative precision of ± 0.0003 % on small volume samples for density, and a relative precision of ± 0.012 % when converted to salinity with an equation of state that accounts for seawater composition.

Here, we test and apply this density-based method to determine bottom water paleosalinity from sedimentary porewater, explicitly correcting for diagenetic composition changes of major ion concentrations, and compare our density-determined profile to titration determined Cl⁻ profiles. We use this data to infer high precision LGM bottom water salinity at a previously unsampled North Atlantic site.

Methods

Overview

Here, we discuss the design, evaluation, and application of a density-based method for determining *in-situ* chloride concentration prior to diagenesis, *[Cl⁻]ᵒ*, which can be used to estimate past bottom water salinity. High precision densities were measured by oscillating U-tube frequency analysis, similar to the approach Millero et al. (2008) developed for water column samples. We extend their technique to account for the effect of diagenetic addition and removal of solutes on density. These affect both the mass and volume of the solution. Based on these experiments, we developed an analytical protocol for porewater sample analysis.

We convert measured density, ρ_{meas}, to *[Cl⁻]ᵒ* based on the 2010 equation of state for standard seawater (which relates density, salinity and temperature)(Mcdougall et al. 2009), correcting for the density effects of diagenesis

$$[Cl^-]^o = \frac{\rho_{meas} - \rho_{H_2O}}{a + \sum_i \Delta R_i Ar_i - \rho_{meas} \sum_i \Delta R_i V_i} \qquad (1.1)$$

(see *Table 1.1* for symbol definitions). The index *i* refers to each non-conservative solute with a significant contribution to salinity whose ratio to Cl⁻ may differ from that

in standard seawater on which the equation of state is based. Values for constants in

equation 1.1 are provided in *Table 1.2*.

Porewater Cl⁻ concentration *[Cl⁻]* will differ slightly from *[Cl⁻]ᵒ* if diagenesis has

affected the volume of solution. Equation 1.2 shows the measured density to *[Cl⁻]*

conversion relevant for direct comparison to titration determined *[Cl⁻]* and diffusion

modeling. The denominator contains the density of pure water ρ_{H2O}, rather than the

measured porewater density.

$$[Cl^-](z,0) = \frac{\rho_{meas} - \rho_{H_2O}}{a + \sum_i \Delta R_i Ar_i - \rho_{H_2O} \sum_i \Delta R_i V_i} \tag{1.2}$$

Throughout this manuscript, we denote *[Cl⁻]* in terms of depth below seafloor *z* and

time *t* with the syntax *[Cl⁻](z,t)*, where bottom water is *[Cl⁻](0,t)* and modern porewater

is *[Cl⁻](z,0)*. Modern porewater immediately below the seafloor is equivalent to

modern bottom water *[Cl⁻](0,0)*.

[Cl⁻](z,0) is calculated at each depth below the seafloor (bsf) for which

porewater density and major ion concentrations were measured. To minimize the

effect of procedural errors, relative solute ratio *ΔR_i* values at each depth are based on

profiles smoothed by depth-weighted averaging. Uncertainty in the major ions and

density-based *[Cl⁻](z,0)* is determined through a Monte Carlo analysis. Our approach

yields a high precision profile that can be used to model the evolution of porewater

chloride, following the methods of Adkins and Schrag (2003), from which past bottom

water salinity can be inferred.

Density Measurement Evaluation and Experimental Design

Instrumental Precision and Optimum Operating Temperature

The Anton Paar DMA 5000 M Density Meter measures the frequency of oscillation (by optode) of a liquid or gas sample injected into a borosilicate glass U-tube kept at a nearly constant temperature (measured to $\pm 0.001^\circ$C). Since oscillatory frequency depends on mass, the DMA 5000 determines density by comparing the frequency of the U-tube to an internal reference. Before sample analysis, the instrument is calibrated by measuring laboratory air and 18.2 MΩ Milli-Q^{TM} deionized water (DI), which has an advantage over seawater standards as its density is independent of evaporation and differs from seawater's by only 2.5 %. A seawater reference produced by the International Association for Physical Sciences of the Ocean (IAPSO) is measured to assess calibration accuracy.

The DMA 5000 is ideal for high precision porewater analysis as the U-tube volume is only 1.2 cm^3, sample recovery is possible after the non-destructive measurement, and the density is measured to a precision of approximately 10^{-3} kg/m^3. Additionally, the DMA 5000 is relatively insensitive to ship motion. This high precision is achieved by averaging internal replicate measurements of temperature and density in rapid sequence to a single value for each injection (see Figure A1 for measurement nomenclature).

To determine an optimum operating temperature, instrument reproducibility was assessed at six different internal temperatures (5, 10, 15, 20, 25, and 30 °C), where each experiment consisted of 30 injections from a single batch of air

equilibrated DI at lab temperature. DI was injected into the U-tube from a 12 cm^3 high-density polyethylene syringe (with no needle attachment) and 10 internal replicate measurements were performed in five minutes. The temperature variation between replicates was lowest when the instrument temperature was set close to lab air temperature (20 °C). The standard deviation of the 30 measured DI injections was 4.7 x10^{-4} °C for temperature and 2.1 x10^{-3} kg/m^3 for density at 20 °C.

Minimizing Bubbles and Sample Volumes

Feistel et al. (2010) noted in their density analyses of filtered Baltic Sea seawater that the largest source of error is the intermittent presence of bubbles in the measured solution. To overcome this problem they degassed each sample by drawing it into the injection syringe through a hypodermic needle. We developed a version of their protocol for degassing small samples and tested its efficacy in experiments where 6 replicates of both DI and filtered seawater were extracted into 12 cm^3 syringes through hypodermic needles. After removing the needle, 3 cm^3 increments were injected into the U-tube without detaching the syringe, with 5 internal replicate density measurements performed on each injection. The standard deviation of the 6 DI injections (internal replicate averages of second injections) was 4.1 x10^{-3} kg/m^3, indicating that degassing before injection achieves similar reproducibility with smaller volumes and considerably less replicates than extracting without a needle. As the filtered seawater standard deviation (internal replicate averages of all injections) was 5.9 x10^{-3} kg/m^3 when 12 cm^3 of sample is analyzed, we can further reduce the sample size (fewer injections per sample) and still achieve unprecedented precision.

We also evaluated reproducibility for small sample volumes (3 cm^3) through six analysis sequences, each containing one DI standard followed by four identical seawater samples. Sample or DI was extracted into a 12 cm^3 syringe through a hypodermic needle and measured in two injection of 1.5 and 1.2 cm^3, respectively. Since the first sample injection is only 0.3 cm^3 greater in volume than the U-tube volume, very little rinsing occurs during injection and carry-over was observed between the DI standard and the first seawater sample. Following the identification of this problem we rinsed the U-tube with 12 cm^3 of filtered seawater between any analysis of a DI standard and a seawater sample or standard. We continued to use a 12 cm^3 syringe for the DI extraction and to measure two injections of 6 and 3 cm^3 respectively, effectively rinsing the U-tube before analyzing the standard. Five internal replicates, measured over three minutes, were averaged to a single representative measured density of each injection.

No drift correction was applied, as the slope of a linear regression fit to measured DI density as a function of time was statistically indistinguishable from zero. The standard deviations of the small volume DI and filtered seawater injections were 4.1 x10^{-3} and 10 x10^{-3} kg/m^3 respectively, where the higher error in seawater is likely due to carry-over between different solution types. Considering the low drift and high carry-over observed during the experiment, we recommend the following analysis sequence: 1 DI standard, U-tube rinsed with 60 cm^3 of filtered seawater, 10 samples. To maximize sample processing efficiency, we reduced the number of internal replicates to five, as the standard deviation of 10 internal replicates was less than 10^{-3}

kg/m^3 in all experiments. See the diagram in Appendix 1.A for a detailed breakdown of our recommended porewater density analysis sequence.

To further improve the reproducibility of sample replicates, we evaluated the use of Vacutainers™ as sample vials. Storing seawater in evacuated containers facilitated degassing prior to and minimizes the pressure decrease during extraction through a hypodermic needle into the syringe. While dissolved gases potentially affect the density of solution, de-gassing samples via this technique conveniently does not measurably affect density for N_2, O_2 and Ar since the density change due to loss of mass is almost exactly compensated by the loss of volume (see Appendix B for full calculation).

Seawater test samples were extracted from Vacutainers™ and analyzed for density, interspersed with one DI standard every four samples. This analysis sequence was repeated five times. Instrument drift, observed during this experiment, was assessed by fitting a linear regression (measured density as a function of time) to all DI standards analyzed over the course of the experiment. Sample densities were drift corrected by normalizing to a DI standard density predicted from the linear fit. The standard deviation of the drift corrected densities of seawater test samples stored in Vacutainers™ was 8.9 x10^{-3} kg/m^3, an 11 % improvement from needle-only degassed samples (10 x10^{-3} kg/m^3). We applied this optimized protocol, with reduced bubbles and minimal drift, to porewater density analyses performed in this study, since it is expected that due to temperature dependence of solubility, these samples will have total dissolved gas pressures in excess of one atmosphere at laboratory temperature.

To identify error introduced by bubbles, we assessed their effect on the reproducibility of the internal replicate density measurements. During all method development experiments, the standard deviation of the internal replicates was noted for any injection where a bubble was visible in the instrument's U-tube viewing window. These standard deviations were compared to those of injections with no visible bubbles to determine a standard deviation used to identify injected solutions likely to contain bubbles, even when bubbles are not visible through the viewing window, 9×10^{-3} kg/m^3. We call this the "bubble threshold". Injections with standard deviations of the internal replicates greater than the bubble threshold are excluded from processing.

Site Description and Sample Collection

We collected the samples for this study on expedition KN223 (cruise doi: 10.7284/900427) of *R/V* Knorr from co-located Sites 03 and 10 (14.4007 ^{o}N, 50.6228 ^{o}W, 4453 m water depth, see *Figure 1.1*) using a rosette-mounted Niskin Bottle (CTD), multi-core (MC), and long piston core (LC) (Curry et al. 2008). Long core samples were recovered from the seafloor to 28.66 and 32.22 meters below sea floor (mbsf) at Sites 03 and 10, respectively. Lithology is relatively uniform, alternating between nannofossil clay and clayey nannofossil ooze, with approximately 100 m of sediment (Divins et al. 2003) overlying 40 Ma crust (Müller et al. 2008).

Bottom water gathered from CTD samples collected within 20 m of the seafloor and MCs that captured water overlying minimally disturbed surface sediment was filtered through 0.45 μm polysulfone disposable filters (Whatman Puradisc PES).

LC subsamples (10 cm long) were sliced from the core at approximately 60 cm intervals. Porewater was extracted with hydraulically driven titanium squeezers (modified after Manheim et al. (1974)) and filtered through 0.45 μm polysulfone disposable filters (Whatman Puradisc PES). Shipboard analyses include titration-determined Cl^- concentration, SO_4^{-2}/Cl^- ratio, alkalinity (ALK), pH, dissolved inorganic carbon (DIC), porewater and bulk sediment density, and formation factor (data doi: 10.26022/IEDA/111472). Cation concentrations (Na^+, Mg^{+2}, Ca^{+2}, K^+) were determined after the expedition by ion chromatography (*Figure 1.2*) at the University of Rhode Island Graduate School of Oceanography.

Analyses

Density Analysis

Porewater density was quantified shipboard with the DM 5000, calibrated with DI. IAPSO batch P156 standard seawater (Millero et al. 2008) was used as a quality check. Samples were first injected into and stored in 15 cm^3 Vacutainers™. They were then extracted into 3 cm^3 hypodermic syringes to facilitate degassing before injection into the DM 5000. Each sample was extracted from its Vacutainer™ in triplicate (three separate syringes) to minimize degassing artifacts. Each individual triplicate was measured twice, two discrete injection replicates (1.5 and 1.4 cm^3 each), with the density of each injection averaged from five replicate density measurements (see Appendix 1.A for a flow diagram). A fourth extraction was performed when bubbles were detected in the U-tube during one of the initial triplicate injections. The final density value for each sample was calculated from the three highest precision

injection averages (determined based on the standard deviation of injections from the same syringe), excluding any bubble-biased values. The relative standard deviations of DI and IAPSO injection averages were 0.0002 % and 0.0006 % respectively for the 27 DI and 7 IAPSO standards measured while analyzing Site 03 samples. IAPSO standard salinity determined by density measurement converted with the equation of state (34.971 g/kg) differs from the standard's certified salinity of 34.994 g/kg by only 0.07 % (see *Table 1.2* for details). The pooled standard deviation represents overall error for the dataset including individual measurement error and the relation of neighboring measurements (Berlekamp 1997). The relative pooled standard deviation of the Site 03 porewater density samples was 0.0006 %, identical to the precision of the seawater standard.

Chloride Titrations

We determined Cl^- by $AgNO_3$ titration of 1 cm^3 of the pore fluid. All titrations were performed in duplicate using a Metrohm 794 Basic Titrino autotitrator, Metrohm Ag Triode, and nominally 0.1 M $AgNO_3$ titrant. Reagent standardization was based on replicate analysis of IAPSO batch P156. Equipment, standards, and replicate protocols were identical for both shipboard and post-cruise analyses, except post-cruise titration aliquots were weighed (Mettler Toledo AG 245, 0.02 mg repeatability) rather than pipetted (1 mL adjustable volume Eppendorf^{TM} with ep tips) to increase analytical precision. The relative standard deviation of the 55 IAPSO standards titrated shipboard was 0.15 %. The pooled percent standard deviation of Site 10 samples was 0.17 % when analyzed shipboard and 0.11 % when analyzed post-expedition, demonstrating

the higher precision possible when titrating weighed aliquots. Profiles from post-expedition titration of weighed samples have consistently higher *[Cl⁻]* than profiles from shipboard titration of pipetted samples, indicating evaporation (*Figure 1.3*).

Major Ion Chromatography

Major ion concentrations or ratios were quantified based on peak areas measured with a Metrohm 861 Advanced Compact Ion Chromatograph (IC). The IC was comprised of a Metrohm 853 CO_2 suppressor, a conductivity detector, and a 20 µL injection sample loop with a Metrohm 837 IC Eluent/Sample Degasser coupled to the system with the column oven set to 32 °C. SO_4^{-2}/Cl^- ratios were quantified using a 150 x 4.0 mm Metrosep A SUPP 5 150 column with 3.2 mM Na_2CO_3, and 1.0 mM $NaHCO_3$ eluent, while cation (Na^+, Mg^{+2}, Ca^{+2}, K^+) concentrations were quantified using a Metrohm C6 250/4.0 column with a C4 guard column and 4 mM nitric acid, 0.4 mM dipicolinic acid eluent.

All porewater samples and IAPSO quality controls were diluted 1:50 with DI. Prior to analysis, a working standard was created in a single large batch 1:50 dilution of IAPSO with DI and calibrated against individually pipetted dilutions of IAPSO. Samples were analyzed interspersed with working standards and quality controls in each analytical batch (a sequence of 36 chromatograms). In each batch five quality controls were included to quantify external reproducibility and test for systematic concentration offsets. All samples and IAPSO quality controls were diluted using the same pipettes as were used to calibrate the working standard (10 cm³ Dispensette™ and 200 fixed volume Eppendorf™ with ep tips). Each analytical batch was drift-

corrected based on a first or second order least square fit to the peak areas of the working standard versus time.

Measured SO_4^{-2} and Cl^- peak areas were ratioed before calibration to the working standard since their errors correlate (see Appendix 1.A). The relative standard deviation of drift-corrected IAPSO SO_4^{-2}/Cl^- ratios was 5.2×10^{-2} % for all KN223 analyses (n=79).

Cation concentrations were calculated directly from measured peak areas of sample relative to the working standard for only the ion of interest, as the four cations evaluated had uncorrelated errors. The relative standard deviation of drift-corrected IAPSO cation concentrations were 0.31, 0.81, 2.2 and 1.2 % of the measured value for Na^+, Mg^{+2}, Ca^{+2}, and K^+ respectively (n=66). Measured quality controls are shown compared to their reference values in *Table 1.2*. The pooled standard deviations of measured porewater samples relative to reference values were 0.29 % for Na^+, 0.51 % for Mg^{+2}, 1.3 % for Ca^{+2}, and 1.1 % for K^+. These quantified precisions are consistent with those of measured seawater standards.

Alkalinity and Dissolved Inorganic Carbon

ALK was determined via Gran titration (Edmond 1970) using a Metrohm 809 Titrando autotitrator and nominal 0.1N HCl, calibrated with Dickson CRM seawater standard (Marine Physical Laboratory, Scripps Institution of Oceanography, Batch 156, certified ALK 2232.58 ± 29 µmol/kg, DIC 2040.94 ± 0.41 µmol/kg). A drift standard was analyzed after every five samples. The standard deviation of the 92 drift standards analyzed during the expedition was 0.75 %.

DIC concentration was measured with a Marianda AIRICA™ system consisting of a syringe module, a sample stripping manifold, and a LICOR LI-7000 CO2/H2O infrared analyzer. Porewater sample or standard was acidified in the stripper with three 50 μL strokes of 10 % phosphoric acid. The CO_2 was stripped from the sample with N_2 and dried using a series of two Permapure Nafion tubes and a cooling chamber before measurement of infrared absorption due to CO_2. The CO_2 absorption was integrated to determine the total CO_2 stripped from the sample, applying the Beer-Lambert law (Swinehart 1962). A single determination consisted of three separate 1 cm^3 injections of sample or standard where each injection was preceded by two 1.1 cm^3 rinses of the stripper. Due to carryover, the first injection was discarded, and the remaining two averaged to calculate DIC concentration from the integrated absorption of the sample relative to the standard. DIC concentration uncertainty was 0.32 % of the measured value, calculated as the standard deviation of the Dickson standards (n=125).

Porewater bicarbonate concentration [HCO_3^-] was calculated according to carbonate equilibrium from the ALK and DIC measured shipboard immediately after squeezing (Edmond and Gieskes 1970; Pilson 2015).

Formation Factor and Porosity

Accurate time dependent modeling of pore water chemical profiles requires inclusion of accurate and precise tortuosity profiles. Diffusive tortuosity θ^2 can be evaluated as a function of depth by measuring porosity ϕ and formation factor f shown in equation 1.3 (McDuff, Gieskes, and Lawrence 1978).

$$f = \frac{\theta^2}{\phi} \qquad\qquad (1.3)$$

Porosity was calculated from bulk and porewater densities measured shipboard and sediment densities obtained from literature. Bulk density was measured by gamma ray attenuation on the multi-sensor track, where whole rounds not used for shipboard analyses were scanned upon recovery. Porewater densities measured as described above were averaged and converted to an *in-situ* density at subseafloor temperature and pressure (1029.6 kg/m^3). KN223 Site 03 and 10 sediments are predominantly nannofossil clay, with a dry density of 2656 kg/m^3 (measured at nearest International Ocean Drilling Site, Erbacher et al. 2004; Pälike et al. 2013). As lithologies are consistent, using a constant literature value for sediment density does not have a significant impact on precision.

Formation factor was measured by conductivity shipboard using a Metrohm/Brinkman Conductometer with a custom-built probe containing two electrodes 1 cm apart. After core sections had been split lengthwise and equilibrated to room temperature, conductivity was measured at 20 cm intervals by inserting the Conductometer's two electrodes into the sediment of the exposed core interior. The probe was rinsed with DI water between measurements and a standard consisting of 0.2 μm-filtered bottom water was analyzed every five measurements to allow for instrument drift corrections. Temperature measurements accompanied each sample interval and final conductivity values were normalized to 25 °C. The formation factor

was calculated as the ratio of the bottom water conductivity to that of the bulk sediment. Physical property plots are included in Appendix 1.C.

Profile Smoothing and Error Evaluation

Density, major ion concentration, and physical property profiles are smoothed using a second order robust-weighted local regression (rLoess) with a span of 60 % depth (Cleveland and Devlin 1988). The difference between the measured and rLoess fit values at each depth is used to determine the profile standard deviation (error due to both sample collection and analysis for an individual sample) of each measured parameter. Outliers, defined as greater than twice the standard deviation from the rLoess calculated value at a given depth, are replaced with the rLoess value to produce an outlier filtered profile (denoted with the subscript $_{meas}$). The same rLoess technique is applied to this filtered profile (excepting replaced outliers) to produce a smooth fit, shown in *Figure 1.2*.

We applied a Monte Carlo technique to assess uncertainty of the density and major ion concentration profiles (known to be smoothed *in-situ* by diffusion) as a function of depth. At each depth, a normally distributed random number was generated with a standard deviation of twice the filtered profile standard deviations and centered on the filtered rLoess smoothed value. This process was repeated 100 times for each measured value, producing 100 Monte Carlo profiles that are collectively representative of the expected uncertainty in the original profile (Figure A2). Each Monte Carlo profile was smoothed with an rLoess fit and these values were averaged at each depth. Uncertainty was assessed as the standard deviation of the

Monte Carlo smoothed values at that depth, centered on their average (shown as error bars on *Figure 1.2*).

Chloride from Porewater Density

Diagenetic changes to porewater density are quantified using relative solute ratios ΔR_i and equation 1.4 to determine porewater chloride concentration from density.

$$\Delta R_i = R_i - R_i^o = \frac{[i]}{[Cl^-]} - \left(\frac{[i]}{[Cl^-]}\right)^o \tag{1.4}$$

As we expect the *in-situ* porewater solute profiles to have been smoothed by diffusion, the rLoess smoothed values are used to calculate the relative solute ratios at each depth where density was measured (see Appendix 1.B).

Solutes which contribute at least 0.01 % to porewater salinity were measured as described above and evaluated with equation 1.4, while those solutes present at concentrations lower than this threshold are not evaluated as their effect on density is not statistically significant within the measurement uncertainty. Silica, for example, is low (less than 0.0001 mol/kg) in deep ocean sediment porewaters of similar lithology and temperature to Sites 03 and 10 (Andrews and Hargrave 1984; Schink, Fanning, and Pilson 1974) and is not measured directly in our study. At other locations, including continental shelves or estuaries, silica reaches concentrations in sediment porewater of up to 0.001 mol/kg (DeMaster 2002; Gehlen and Van Raaphorst 2002; Willey and Spivack 1997). Silica's contribution to salinity at Sites 03 and 10 is less than 0.008 %, well below the uncertainty of our density measurement, and at locations

with high porewater silica increases to 0.08 % of salinity and silica can be measured

for inclusion in the density technique.

Porewater chloride concentration $[Cl^-](z,0)$ is used to determine ΔR_i for solutes

not measured as a ratio to chloride (everything except SO_4^{-2}). To avoid introducing

uncertainty associated with titration measured $[Cl^-]$, initial porewater $[Cl^-](z,0)$ is

determined from smooth measured densities using the equation of state (Mcdougall

et al. 2009) without accounting for diagenesis (porewater treated as standard

seawater composition). This initial porewater $[Cl^-](z,0)$ is used for the first

determination of ΔR_i and replaced with the density determined value of $[Cl^-](z,0)$ after

each subsequent iteration of the density to $[Cl^-](z,0)$ conversion (equations 1.2, 1.4;

see Appendix 1.B for full derivation).

Adjusting density for the ΔR_i of solutes that experience limited diagenesis

(effectively conservative) introduces error through the uncertainty associated with

that solute's concentration measurement. To distinguish solutes effected by

diagenesis from conservative ions, we examine the charge balance anomaly B for each

sample and the IAPSO quality control standard using equation 1.5.

$$B = [Na^+] + [K^+] + 2[Mg^{+2}] + 2[Ca^{+2}] \qquad (1.5)$$

$$-[Cl^-] - 2[SO_4^{-2}] - [HCO_3^-]$$

Solute i is considered conservative if the average of B across all depths decreases upon

replacing solute i's smooth measured concentrations with concentrations determined

from $[Cl^-](z,0)$ and R_i. At Site 03, the charge balance anomaly averaged over all depths

is 3.2 mM for all solutes and -1.2 mM when Na$^+$ is treated as conservative. All solutes

with potential for diagenesis were evaluated, and only Na^+ does not experience significant diagenesis and is subsequently considered conservative and excluded from the density to chloride conversion for Sites 03 and 10.

$[Cl^-](z,0)$ is calculated from the filtered, unsmoothed measured density and the iterated smoothed ΔR_i profiles of non-conservative solutes (Eq. 1.2, 1.4; full derivation Appendix 1.B). Between salinities 34.8 and 35.8 g/kg, density is a linear function of $[Cl^-]$ (Mcdougall et al. 2009). Equation 1.2 is based on this linear relationship, while also including the effects of diagenetic changes on volume of solution and mass of non-conservative solutes. This linear fit of density as a function of $[Cl^-]$, using the full thermodynamic equation of state at 20 ℃ and 1 atm, has a slope a of 4.6519 x10^{-2} kg/mol and an intercept ρ_{H2O} of 998.75 ± 0.01 kg/m^3 where uncertainty is determined as the 95 % confidence limit. $[Cl^-](z,0)$ is calculated with equation 1.2, then used as the input to equation 1.4 on each subsequent iteration, until $[Cl^-](z,0)$ no longer varies between input and output from equation 1.2. $[Cl^-](z,0)$ from the final iteration is shown in *Figure 1.3* with its uncertainty evaluated through the same Monte Carlo technique applied to titration determined $[Cl^-](z,0)$ (described above).

Modern Porewater Chloride

To relate our measured porewater $[Cl^-](z,0)$ to past bottom water chloride concentration $[Cl^-](0,t)$ we account for the diffusive smoothing of $[Cl^-](z,t)$ that occurs over time through one-dimensional numerical diffusion modeling as pioneered by Adkins and Schrag (2003). $[Cl^-](z,t)$ over depth and time is modeled using equation 1.6,

where $\phi(z)$ is the porosity, $D(z)$ is the seawater Cl⁻ diffusion coefficient, and $f(z)$ is the formation factor at depth z below seafloor.

$$\phi(z)\frac{\partial[Cl^-](z,t)}{\partial t} = \frac{\partial}{\partial z}\left(\frac{D(z)}{f(z)}\frac{\partial[Cl^-](z,t)}{\partial z}\right) \qquad (1.6)$$

Advection and *in-situ* reaction terms are not included in equation 1.6 as the low sedimentation rate and ash-free lithologies of our sites render them negligible.

Measured formation factors and porosities are rLoess smoothed across measured depths and extrapolated to basement, as the entire sediment column was not sampled at our site (see Appendix 1.C). $D(z)$ is calculated from the free solution Cl⁻ diffusion coefficient (9.60×10^{-10} m²/s); seawater viscosity at 0 °C; the slope of D as a function of temperature (0.438×10^{-10} m²/s°C)(Boudreau 1997); and the near-seafloor temperature gradient at Sites 03 and 10 of 0.05 °C/mbsf (Erbacher et al. 2004).

Diffusion modeled porewater chloride concentrations from present day are optimized to each density or titration measured $[Cl^-](z,0)$ profile by optimizing the boundary condition, ;bottom water chloride concentration over time $[Cl^-](0,t)$. Global sea level over the past 70 ka from Siddall et al. (2008) is normalized and scaled to represent bottom water $[Cl^-](0,t)$. Siddall et al. find the greatest sea level change relative to modern occurring at 21.7 ± 0.17 ka, identified as the LGM. A family of boundary conditions is produced by varying $[Cl^-](0,0)$ across its measured uncertainty and scaling $[Cl^-](0,t)$ to encompass the potential range of salinity changes between modern and LGM (*Figure 1.4*). The initial condition $[Cl^-](z,-70ka)$ is assessed as the average of $[Cl^-](0,t)$ from the modern to LGM. Each boundary condition $[Cl^-](0,t)$ is

used to predict a modern porewater $[Cl^-](z,0)$ using equation 1.6 with depth resolution

of 0.5 m (Δz). Modern $[Cl^-](z,0)$ determined from each diffusion modeled boundary

condition is compared to each of the 100 measurement-based Monte Carlo $[Cl^-](z,0)$

profiles through the sum of their squared differences at each depth, generating a

family of modern $[Cl^-](z,0)$ modeled best fits for each distinct measured $[Cl^-](z,0)$.

Diffusion modeled $[Cl^-](z,0)$ and its uncertainty are determined as the average and

standard deviation of the 100 modeled best fits (*Figure 1.3*, *Figure 1.4*). The

uncertainty associated with the density determined $[Cl^-](z,0)$ includes errors

introduced during sampling, porewater extraction, storage, and analysis.

Bottom Water Paleosalinity

Bottom water chloride concentration and its uncertainty is determined as the

average and standard deviation of the 100 boundary conditions, $[Cl^-](0,t)$, associated

with the porewater chloride best fits for the measured profile of interest. The LGM is

identified in porewater profiles as the peak in $[Cl^-](z,0)$, varying in depth below

seafloor as a function of porosity and initial condition.

To evaluate bottom water paleosalinity we convert $[Cl^-](z,t)$ to salinity , with

equation 1.7 (Lewis and Perkin 1978; Mcdougall et al. 2009; Millero et al. 2008).

$$S(z,t) = 1.80655[Cl^-](z,t)\frac{Ar_{Cl^-}}{\rho_{BW}} \qquad (1.7)$$

Here, Ar_{Cl} is the atomic weight of Cl$^-$ and ρ_{BW} is the measured bottom water density at

laboratory pressure and temperature (20 ^oC). Bottom water salinity change between

the modern and LGM is determined for each measured porewater chloride profile

(Sites 03 and 10, density and titration determined) as maximum modeled bottom water salinity minus the modern measured bottom water salinity, $S(z_{LGM},-21.7ka)$ - $S(0,0)$, reported in *Table 1.3* as an absolute value and a relative change.

Results & Discussion

Seawater Quality Controls

IAPSO seawater quality controls measured for SO_4^{-2}/Cl^-, $[Na^+]$, $[Mg^{+2}]$, $[Ca^{+2}]$, and $[K^+]$ have averages within 0.5 % of their reference values, and average measured density was only 0.01 % (three times the analytical uncertainty) lower than expected from the thermodynamic equation of state. Measured densities of Site 03 bottom water collected by CTD and MC were within 0.02 kg/m^3 of each other, within 0.05 kg/m^3 of the density calculated from the nearest World Ocean Circulation Experiment (WOCE) measured salinity (14.1 ^{o}N, 52.3 ^{o}W, 5050 m, 34.841 g/kg) and the thermodynamic equation of state, and within 0.02 kg/m^3 of the shallowest measured porewater density. These measured and reference values are included in *Table 1.2* for quality controls and sample types.

Seafloor porewater solute ratios measured in the shallowest LC sample differ slightly from standard seawater solute molarities (Millero et al. 2008) at the average measured bottom water salinity (density determined from CTD and MC), shown in *Figure 1.2* and listed in *Table 1.2.* This difference is likely due to Ca^{+2} increase in the porewater from carbonate dissolution and systematic artifacts introduced during squeezing (Manheim 1974)..

Chloride Determination Techniques

Porewater chloride concentration profiles determined from shipboard density, shipboard titration, and post-expedition titration from two adjacent cores (Sites 03 and 10) are compared in *Figure 1.3*. Porewater chloride profiles determined by density have higher precision and reproducibility than those determined by titration, either shipboard or post-expedition. The rLoess smoothed, shallowest measured porewater values *S(0,0)* differ between Sites 03 and 10 by 0.12 % when measured by density and 0.23 % when measured by shipboard titration, with respective uncertainties of 0.009 and 0.027 g/kg (*Table 1.3*). *S(0,0)* differs between Site 10 samples measured by titration shipboard and post-expedition by 0.4 %, demonstrating the evaporative artifacts associated with stored samples (*Figure 1.3*).

The Monte-Carlo determined errors for the concentration datasets were 0.12 % of the measured value for titration determined Cl^-, 0.08 % for SO_4^{-2}, 0.29 % for Na^+, 0.51 % for Mg^{+2}, 1.3 % for Ca^{+2}, 1.1 % for K^+, and 2.75 % for HCO_3^-. We achieved a relative pooled standard deviation of 0.007 % for density. Measuring density on board ship during the expedition minimizes error due to sample storage that accounts for much of the uncertainty in weighed titration determined Cl^-. Cation concentration analyses, however, were performed after the expedition and not measured directly as ratios to sodium. Future work could reduce error introduced into the cation

concentration data from storage-related artifacts by measuring all solute ratios shipboard on separate cation and anion ICs.

Small systematic offsets are present between [Cl$^-$] determined by shipboard pipetted titration, shipboard density, and weighed titration after the expedition for both adjacent cores (*Figure 1.3*). The consistent offset present between Sites 03 & 10 for the measured profiles determined by titration is absent in the density determined profiles, demonstrating the density technique can be more closely replicated across cores.

Paleosalinity Change

Modeled, optimized salinity change from the pre-industrial to LGM is 3.07 ± 0.03 % and 3.65 ± 0.06 % when determined from density and 2.96 ± 0.12 % and 1.96 ± 0.21 % when determined from titration at Sites 03 and 10 respectively (*Table 1.3*). Titration determined salinity changes differ between adjacent cores by nearly twice their magnitude and have uncertainties up to four times those determined by density.

LCs collected from KN223 adjacent Sites 03 (28.66 mbsf) and 10 (33.90 mbsf) did not penetrate to the depth of the LGM chloride peak identified through diffusion modeling (35.5 – 38.5 mbsf). Measured profiles that capture the full sediment column are ideal for diffusion modeling, as LGM chloride peak depth can be identified in the porewater data independent of the diffusion model, providing a further constraint on boundary and initial conditions. As shown in *Figure 1.3*, the shape of the modeled fit and the depth of its porewater chloride maximum, a function of porosity and boundary and initial conditions, differs from the rLoess smoothed measured data. This

is especially apparent for Site 10's titration determined solution, with 1.0 % lower relative salinity change and the LGM chloride peak located 3 mbsf deeper than in the Site 03 solution. When determined by density, Site 10 has a salinity 0.58 % higher and an LGM chloride peak only 1 mbsf deeper than Site 03's solution.

At the modern seafloor, porewater and bottom water are equivalent in terms of salinity. As modern bottom water salinity differs by less than 0.1% between modeled and measured values, we demonstrate that the diffusion model approach is reproducible despite the limitations associated with depth-limited sample recovery and optimizing an independently-controlled profile shape to measured data. We demonstrate this density-based technique's advantages over the currently available titration technique as the smaller uncertainties and more consistent replicates in density determined chloride concentration profiles are maintained in model determined salinity changes between the modern and LGM.

Global mean salinity determined from eustatic sea level change decreases 3.5 % between the modern and LGM (Clark and Mix 2002). Prior to this study, the most precise technique available in the literature for determining location-specific LGM deep ocean salinity was combining porewater titration Cl^- measurements with diffusion modeling. All published LGM values from this technique for sites in the Pacific and Atlantic Oceans total only 9 locations (Adkins et al. 2002; Adkins and Schrag 2003; Insua et al. 2014), and variations between sites are difficult to explain without accounting for methodological uncertainties. Adkins et al.(2002) found a 2.7 − 6.9 ± 0.03 − 0.17 % salinity increase from the pre-industrial to the LGM. They find a

modern bottom water salinity of 34.884 ± 0.005 g/kg at their nearest site to ours, located 16 ° farther north, with a change of 0.954 g/kg from pre-industrial to LGM. Their relative salinity change of 2.7 ± 0.1 % is the smallest of any change they observe and is consistent in both magnitude and uncertainty with Site 03 titration results. Our density technique, however, yielded higher precision relative salinity changes from both adjacent cores, with values closer to the global average determined sea level change. While both density and titration techniques are sensitive to limitations of the diffusion modeling approach (Adkins and Schrag 2003), increasing the precision of the measured porewater [Cl⁻] profile improves bottom water paleosalinity determination.

Conclusions

We demonstrate that a density-based method can determine porewater chloride concentration with to greater precision and reproducibility than the currently available titration technique. This newly developed shipboard technique is unique in its application of density measurements to porewater and is the first technique that accounts for diagenesis-based composition changes to relate porewater and seawater density through the thermodynamic equation of state. Applying both density and titration techniques to two adjacent cores (KN223 Sites 03 and 10) in the North Atlantic, we model the time-dependent diffusive smoothing of porewater Cl⁻ to examine the bottom water salinity of the LGM for each of the four measured profiles. Bottom water salinity change between the modern and LGM was 3.07 ± 0.03 % and 3.65 ± 0.06 % when determined from density and 2.96 ± 0.12 % and 1.96 ± 0.21 % when determined from titration at co-located Sites 03 and 10, respectively.

Discrepancies between adjacent cores can be attributed to sampling disturbance and penetration to depths shallower than the porewater peak representative of higher salinity LGM bottom water (Adkins and Schrag 2003). Density determined bottom water salinity increase from the modern to the LGM is consistent with published values determined from chloride titration and global sea level change (Adkins et al. 2002; Clark and Mix 2002). Measuring density shipboard minimizes error introduced through sample storage that accounts for much of the scatter in the titration determined Cl^-. Applying our method at additional sites has clear potential to enhance understanding of LGM deep ocean salinity.

Tables

Table 1.1. Index of variables, superscripts, and subscripts used in this paper.

Type	Symbol	Description	Unit
Variables	ρ_{meas}	Density, measured	kg/m^3
	m	Mass	kg
	v	Volume	m^3
	Ar	Molecular Mass	kg/mol
	V	Partial Molar Volume	m^3/mol
	$[\ ]$	Concentration	mol/L
	R	Ratio of bottom water concentration to [Cl$^-$]	-
	ρ_{H2O}	Density of pure water	kg/m^3
	a	Slope of [Cl$^-$] vs. density for standard seawater	mol/kg
	S	Salinity	g/kg
	ϕ	porosity	%
	f	formation factor	-
	D	free solution Cl$^-$ diffusion coefficient	m^2/sec
	z	depth	mbsf
	t	time	sec
	ε	Propagated Error	varies
	σ	Measurement Error	varies
	Δ, δ	Difference	varies
	∂	Partial Derivative	varies
Subscripts & Superscripts	i	solute index	
	j	depth index	
	$meas$	measured	
	BW, PW	bottom water, porewater	
	o	initial	

Table 1.2. Properties for seawater and porewater, including measured values (**boldface**), values calculated from the equation of state or equations 1.2 and 1.7 (*italicized*), and values calculated from standard seawater molarities (underlined) at 1 atm and the salinity *S* shown (Millero et al. 2008). The top five rows show values for standard seawater (IAPSO certified standard reference, cert, and measured, meas, values at 20°C); bottom water from the nearest WOCE site (2.3°C); and measured values for CTD, MC, and the shallowest LC samples collected at KN223 Site 03 (20.001°C). Bottom three rows provide the difference between measured bottom water (average of CTD and MC) and porewater; partial molar volume, *V*, of seawater at 25°C from Millero and Huang (2013); and molecular mass, *Ar*, from Millero et al. (2008).

Type	S g/kg	ρ kg/m³	$[Cl]_\rho$ kg/m³	Cl^-	SO_4^{-2}	HCO_3^-	Na^+	Mg^+	Ca^{+2}	K^+
				[i] (mol/m³)						
IAPSO_cert	34.994	*1024.64*	*559.39*	559.26	28.92	2.11	480.41	54.12	10.54	10.46
IAPSO_meas	*34.971*	**1024.779** **± 0.006**	*559.55* *± 0.14*	-	**28.86** **± 0.08**	-	479.07 **± 1.74**	54.39 **± 0.72**	10.51 **± 0.25**	10.49 **± 1.7**
BW_WOCE	**34.84**	*1027.75*	NA	555.05	28.70	2.09	476.80	53.71	10.46	10.38
BW_CTD	*34.807* *± 0.008*	**1024.645** **± 0.006**	*556.86* *± 0.13*	556.27	28.76	2.10	477.85	53.83	10.48	10.40
BW_MC	*34.832* *± 0.006*	**1024.673** **± 0.005**	*557.26* *± 0.10*	556.67	28.78	2.10	478.19	53.87	10.49	10.41
PW_LC(0,0)	*34.765* *± 0.017*	**1024.638** **± 0.006**	*555.44* *± 0.27*	**555.46** **± 0.46**	**28.06** **± 0.07**	**2.54** **± 0.04**	**481.94** **± 1.29**	**51.45** **± 0.29**	**10.49** **± 0.06**	**12.78** **± 0.11**
BW - PW	*0.05*	**0.021**	*0.88*	**1.01**	**0.72**	**-0.45**	**-3.92**	**2.39**	**-0.01**	**-2.38**
				V (m³/mol) or Ar (kg/mol)						
V	35	NA	NA	1.94×10^{-5}	2.18×10^{-5}	2.75×10^{-5}	-8.40×10^{-7}	-1.96×10^{-5}	-1.61×10^{-5}	9.50×10^{-6}
Ar	NA	NA	NA	3.55×10^{-2}	9.61×10^{-2}	6.10×10^{-2}	1.40×10^{-2}	2.43×10^{-2}	4.01×10^{-2}	3.91×10^{-2}

Table 1.3. Salinity, *S(z,t)*, of bottom water (BW) and porewater for the modern (0 ka) and LGM (-21.7 ka) from shipboard titration and density determined chloride profiles (meas) and their diffusion model best fits (mod). Relative change (%) between modern and LGM bottom water salinity is given in the second from right column. Depth of the LGM porewater signature, identified as the modeled porewater salinity peak, is given in the far right column.

Analysis	Site	$S(0,0)_{meas}$ *g/kg*	$S(0,LGM)_{mod}$ *g/kg*	$S(z_{LGM},LGM)_{mod}$ *g/kg*	ΔS_{bw} *%*	z_{LGM} *mbsf*
Titration	3	34.765 ± 0.017	35.769 ± 0.044	35.211 ± 0.013	**2.96 ± 0.12**	35.5
	10	34.634 ± 0.027	35.338 ± 0.075	34.966 ± 0.023	**1.96 ± 0.21**	38.5
Density	3	34.920 ± 0.005	35.957 ± 0.012	35.384 ± 0.004	**3.07 ± 0.03**	35.5
	10	34.870 ± 0.009	36.116 ± 0.021	35.421 ± 0.006	**3.65 ± 0.06**	36.5

Figures
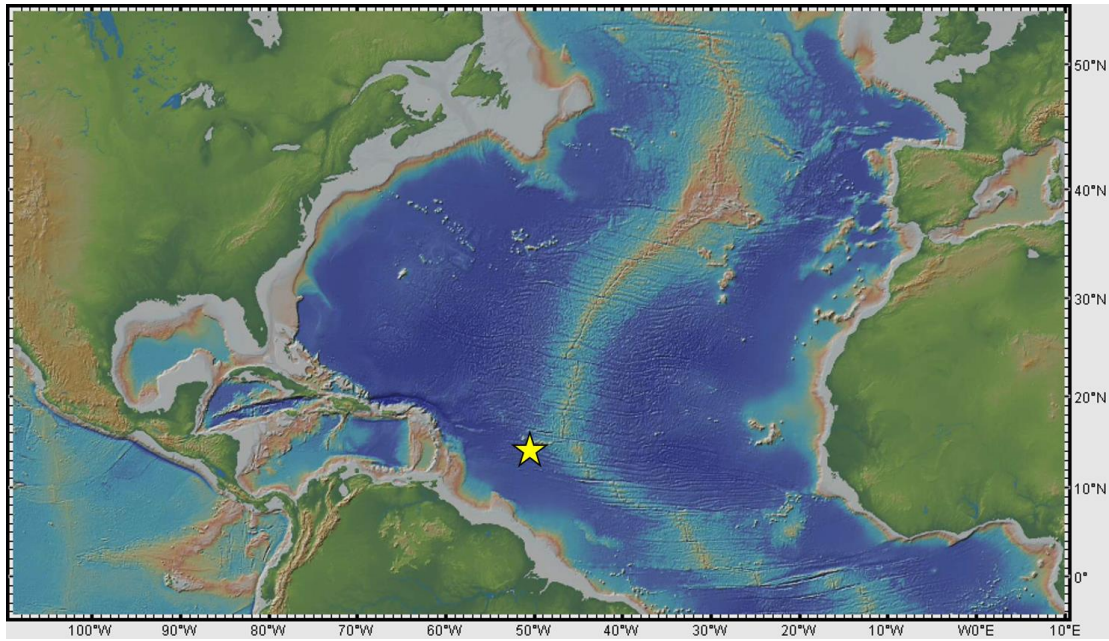
Figure 1.1. Co-located KN223 Sites 03 and 10 (yellow star) where samples were collected.
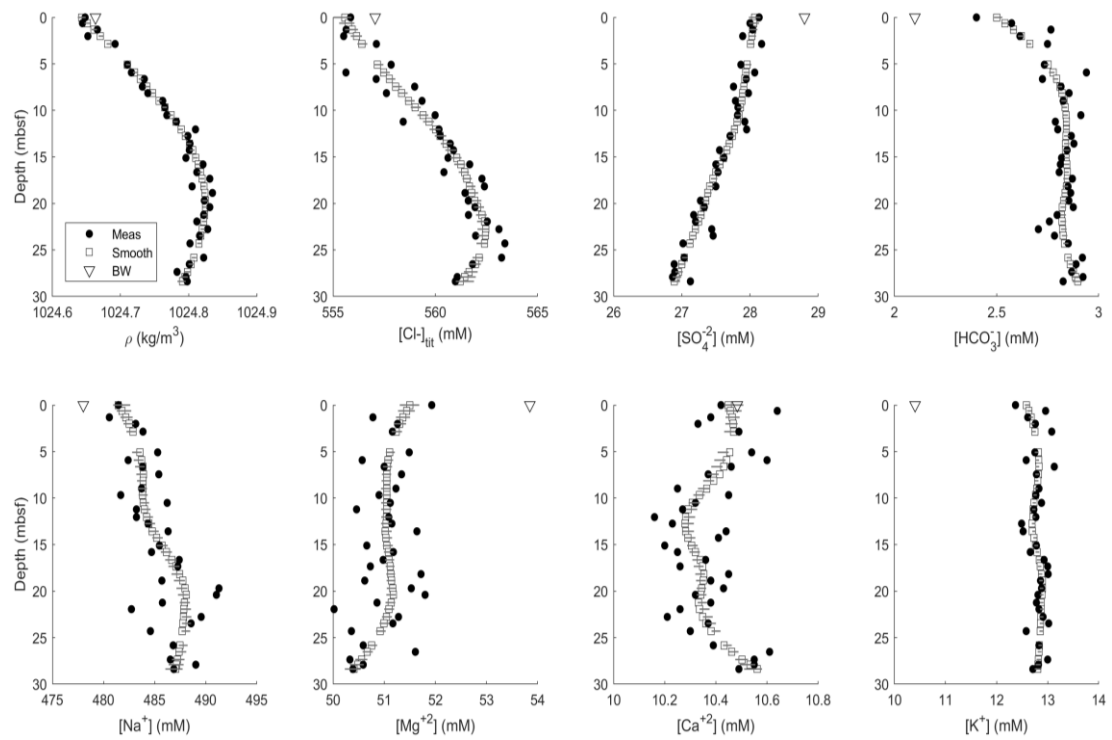
Figure 1.2. Measured profiles from KN223 Site 03, filtered of outliers. Porewater measurements are shown as solid circles with their smoothed (and interpolated where necessary) rLoess fit shown as open squares. Measurement error bars are plotted in gray, centered around Monte Carlo averages. Bottom water values are shown as triangles (average of Site 03 CTD and MC).
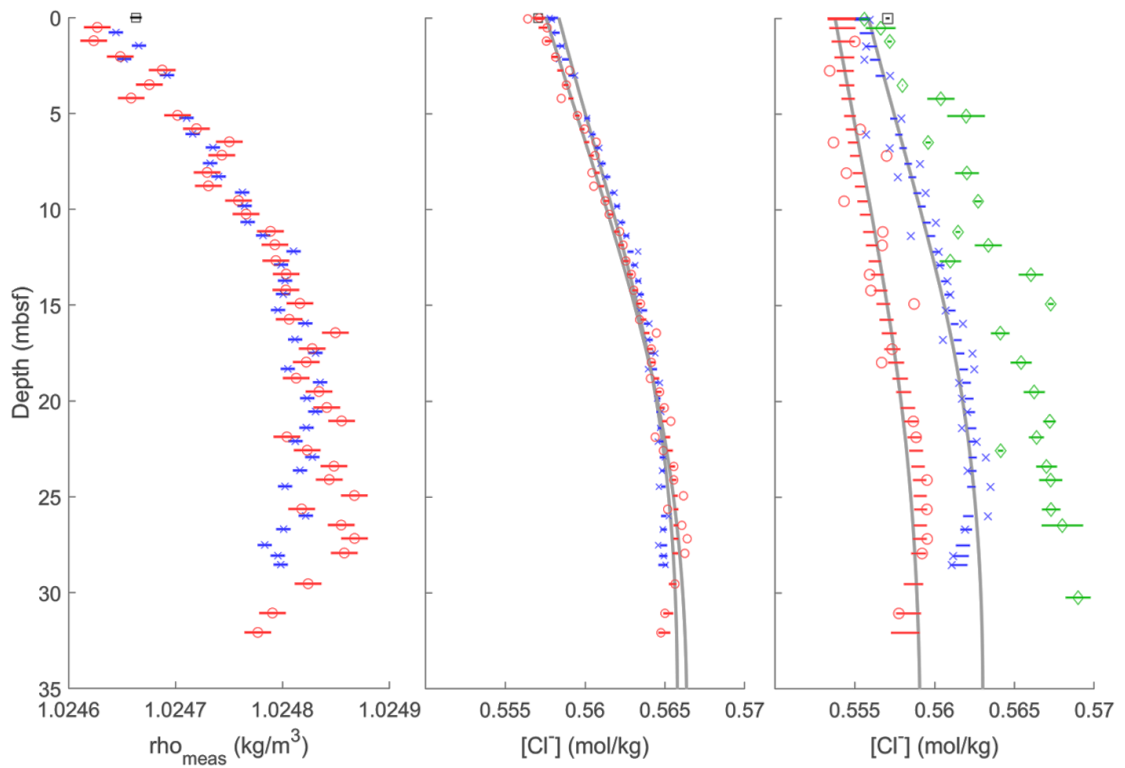
Figure 1.3. Porewater density and chloride from KN223 Sites 03 (blue x's) and 10 (red circles and green diamonds). Chloride is determined from density (center panel) measured shipboard; and titration (right panel) measured shipboard (red x's and blue circles) and post-expedition (green diamonds). Bottom water values (CTD and MC measurement average with standard deviations as error bars) are shown at the seafloor as black squares. Error bars are shown for all discrete values. Gray lines are diffusion model best fits for each profile measured shipboard.
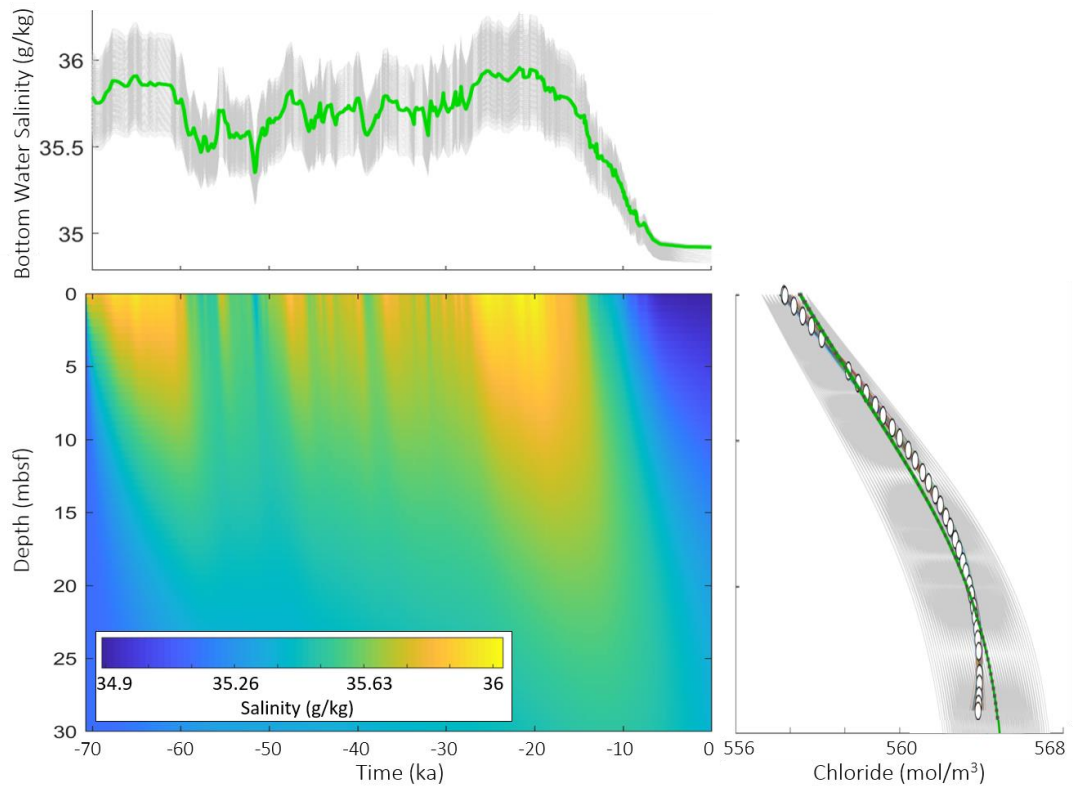
Figure 1.4. Diffusion model optimized to Site 03 density determined chloride. Bottom water salinity over time (top panel), determined from normalized sea level, is input to the diffusion equation with different optimization parameters (gray lines). Modern porewater chloride as a function of depth (right panel) is output from the model (gray lines) and compared to smoothed measured data (white circles). The best model fit is shown over time and depth (center panel), and as a green line in top and right (black error bars) panels.

MANUSCRIPT 2

Deep North Atlantic Last Glacial Maximum Salinity Reconstruction

by

Kira Homola[1], Arthur J. Spivack[1], Richard W. Murray[2], Robert Pockalny[1],

Steven D'Hondt[1], Rebecca Robinson[1]

To be submitted to *Paleoceanography*

---

[1]University of Rhode Island Graduate School of Oceanography
[2]Woods Hole Oceanographic Institution

Abstract

We reconstruct deep water mass salinities and distributions in the western North Atlantic during the Last Glacial Maximum (LGM, 19-26 ka), a period when atmospheric CO_2 was significantly lower than it is today. A reversal in the LGM Atlantic meridional bottom water salinity gradient is observed in several LGM water mass reconstructions and has the potential to increase the thermal energy and carbon storage capacity of the deep ocean, influencing climate, ocean circulation, and atmospheric CO_2.

We reconstruct LGM bottom water salinity based on sedimentary pore water chloride profiles in a north-south transect of piston cores collected from the deep western North Atlantic. We used two methods to determine porewater chloride: one based on density and the other on $AgNO_3$ titration. The density-based method yields up to four times higher precision paleosalinities than the titration-based method. Reconstructed LGM bottom water salinity, determined from the density-based method was $3.07 - 3.65 \pm 0.05$ % higher than modern values at these sites. This inferred increase: i. is consistent with the 3.5 % global average salinity change expected from eustatic sea level rise, ii. confirms a northward expansion of southern deep water, iii. is consistent with shoaling of northern deep water, and iv. supports the argument that there was a reversal of the Atlantic's north-south deep water salinity gradient during the LGM.

Introduction and Background

Meridional overturning circulation (MOC) is an important climate feedback due to its associated heat flux and influence on atmospheric CO_2. Salinity is central to understanding the MOC and is used along with nutrients, dissolved oxygen, and $\Delta^{14}C$ to characterize water mass distributions. MOC is influenced by basin-scale density gradients, with separate northern and southern cells in the Atlantic Ocean (Talley et al. 2015). Presently, Northern Hemisphere deep water formation only occurs in the Atlantic, where warm surface waters flow northward along the western boundary, tilting the east-west density surfaces across the basin (Talley 2011). The thermal wind relationship specifies that on a rotating planet, this zonal density gradient is balanced by a vertical shear in meridional flow, expressed in the North Atlantic as southward return flow of deep water (deeper than ~1km). As north-flowing surface waters release energy to the atmosphere, they increase in density, lose buoyancy, and subduct to form the cold, southward flowing deep waters (e.g. Stewart & Thompson, 2015; Srokosz et al., 2012). This northern cell of Atlantic MOC (AMOC) is vigorous enough to extend south of the equator, entraining southern component deep and intermediate waters and transporting heat northwards across the equator from the Southern Hemisphere (Robinson and Stommel 1959).

Carbon enters the deep ocean through subduction of inorganic carbon-rich cold surface waters, referred to as the *solubility pump*, and export of organic carbon from the surface ocean, referred to as the *biological pump* (Volk and Hoffert 1985). MOC upwelling returns carbon to the surface ocean, where it can be subsequently

released to the atmosphere. Present day North Atlantic surface waters in the region of

deep water formation have initial nutrient and dissolved inorganic carbon (DIC)

concentrations lower than those of Southern Ocean deep water sources, where low

air temperatures drive subduction of denser deep waters fresher than 34.9 g/kg

(Worthington and Wright 1970; W. S. Broecker, Takahashi, and Takahashi 1985;

Woosley, Huang, and Millero 2014). The properties of subducting southern cell waters

vary with Southern Ocean surface conditions including: wind distribution and strength,

sea ice extent, temperature, light, and biological activity (Ferrari et al. 2014). Carbon

sequestration in the southern cell increases with elevated biological uptake, enhanced

air-sea disequilibrium conditions that inhibit carbon release to the atmosphere, or

expansion of its carbon-rich deep waters (Clark and Mix 2002; Watson and Garabato

2006). The relative sizes of the deep water masses, or *standing volume effect*, drives

changes in the efficiencies of both the biological and solubility pumps independent of

changes in overturning or carbon export rates (Skinner 2009). Carbon partitioning

between the atmosphere and deep ocean is regulated by these biological and physical

mechanisms, both of which are interconnected with the MOC (Boyle and Keigwin

1982; Sarmiento and Gruber 2002; Toggweiler and Russell 2008).

Global climate has cycled between major glacial and interglacial modes over at

least the past 730 ka, with changes in atmospheric CO_2 concentrations highly

correlated to climate variations (Petit et al. 1999; Siegenthaler et al. 2005). CO_2

transfer between the atmosphere and deep ocean is an important positive feedback

of glacial-interglacial climate change (Schmittner and Galbraith 2008; Sigman and

Boyle 2000). The deep ocean contains more than 50 times the carbon of the atmosphere, so small ocean carbon inventory changes have large relative effects on the atmosphere (Boyle and Keigwin 1985; Broecker, Clark, and Barker 2008). Changes in the distribution and composition of Atlantic northern and southern deep water masses influence the global carbon inventory and can be constrained through historical reconstructions of water mass geometry. The Last Glacial Maximum (LGM) occurred between 19 – 26 ka and is a critical analog for present day anthropogenic atmospheric CO_2 change, with atmospheric CO_2 concentrations 30% lower than pre-industrial levels (Clark et al. 2009; Mix et al. 2001; Peltier and Fairbanks 2006).

LGM deep water mass distributions, properties, and ages have been examined through measurements of benthic foraminiferal $\delta^{13}C$ and $\delta^{18}O$ (Graham et al. 1981; W. B. Curry and Oppo 2005; Lynch-Stieglitz et al. 2007; Govin et al. 2009; Keigwin and Swift 2017), paleosalinity (Adkins et al. 2002; Adkins and Schrag 2003; Insua et al. 2014; Sijinkumar et al. 2016), and $\Delta^{14}C$ of benthic foraminifera and uranium-thorium dated coral (Burke et al. 2015; Keigwin 2004). Measured results have been contextualized through numerous modeling studies (Cutler et al. 2003; Lund, Adkins, and Ferrari 2011; Clark et al. 2012; Miller et al. 2012; Ferrari et al. 2014; Nadeau, Ferrari, and Jansen 2019), including a comprehensive approach by Galbraith and Lavergne (2019) that found density differences between northern and southern deep water formation regions can be used to predict changes in deep water mass volumes. Matsumoto et al. (2015) identify the potential boundary between LGM northern and southern cells from the transition of enriched (northern) to depleted (southern) $\delta^{13}C$

of LGM benthic foraminifera (Curry & Oppo, 2005). Shown in *Figure 2.1*, the southern

cell expanded farther north and the northern cell shoaled, relative to present day,

increasing the volume of carbon rich water in the deep ocean (Skinner 2009).

Southern component standing volume increase has the potential to account for two

thirds of observed atmospheric CO_2 decrease during the LGM (Brovkin et al. 2007;

Kobayashi, Abe-Ouchi, and Oka 2015) when combined with enhancement of the

Southern Ocean biological pump and increased ice cover amplifying the air-sea

disequilibrium (Ito and Follows 2013).

As the global ocean salt content has been relatively constant over the past 3.2

Ma (Pilson 2015), eustatic sea level 130 m lower during the LGM would result in 3.6 ±

0.3 % average salinity increase relative to pre-industrial (Clark et al. 2009).

Sedimentary pore fluid chloride, determined by $AgNO_3$ titration, combined with

diffusion modeling, has been used to measure LGM bottom water paleosalinity at

several sites in the Atlantic and Pacific (Adkins et al. 2002; Insua et al. 2014). Adkins,

McIntyre, and Schrag (2002) find a 3.5 ± 0.5 % average and 4.2 ± 0.5 % range for

salinity increase from the modern to LGM between their three Atlantic sites (*Figure

2.2*), with a north-south reversal in salinity gradient relative to the modern. This

salinity reversal, where southern sourced deep waters are saltier than deep water

formed in the North Atlantic, is consistent with water distributions inferred from other

proxy measurements and models. Low atmospheric CO_2 and low temperatures result

in decreased precipitation and increased sea ice formation, export, and brine rejection

(Boyle 2002; Jansen 2017). The LGM Southern Ocean is net salinifying, rather than net

freshening as in the modern (Galbraith and Lavergne 2019). Expanded LGM ice sheets increase the salinity and volume of southern deep water and the overturning rate of colder, fresher water in the North Atlantic (Galbraith and Lavergne 2019; Holloway et al. 2016; Jansen and Nadeau 2016; Kwon et al. 2012; Negre et al. 2010). Salinity stratifying the deep ocean increases its thermal energy and carbon storage capacity, likely contributing to many observed climate variations including lower glacial atmospheric CO_2 and Dansgaard-Oeschger events (Adkins, Ingersoll, and Pasquero 2005; Bouttes, Roche, and Paillard 2009; Schmittner and Galbraith 2008). Accurate values of deep water salinities during the LGM are thus critical to constraining MOC. Keigwin and Swift (2017), using foraminiferal $\delta^{13}C$ and $\Delta^{14}C$, find evidence of a northern sourced, low-nutrient abyssal water mass sinking below primary northern deep water (*Figure 2.1*), that could contribute to increased convection and carbon sequestration. While Adkins, McIntyre, and Schrag (2002) measure LGM salinity at 55 ^{o}N and 50 ^{o}S, their values are significantly higher than model results (Galbraith and Lavergne 2019) and represent an unconfirmed (Wunsch 2016)upper bound (Adkins et al. 2002). Because the complex interface between the northern and southern overturning cells during the LGM remains unconstrained in the literature (Sigman, Hain, and Haug 2010), resolving this critical bottom water salinity gradient will require higher resolution data than currently available, both in terms of precision and number of sites. We determine paleosalinity at four sites along a north-south transect in the western North Atlantic (*Figure 2.2*) using our newly developed high precision density-based method (Homola Dissertation 2019, Chapter 1) to assess whether our sites'

paleosalinities are consistent with a northward expansion of southern deep water, a shoaling of northern deep water, and/or a north-south reversal of the Atlantic meridional deep water salinity gradient during the LGM.

Methods

We apply our density-based method for determining *in-situ* chloride concentration [Cl⁻] to four sites in the western North Atlantic. Chloride is measured by titration for comparison at these and two additional sites that could not be assessed through the density-based method due to their high organic content. We generate a diffusion model for bottom water salinity over time and select the best fit to each chloride profile to determine LGM bottom water salinity.

Site Description and Sample Collection

Samples used for this study were collected from *R/V Knorr* during expedition KN223 (cruise doi: 10.7284/900427)(see *Figure 2.2* and *Table 2.1*) using a Niskin Bottle (CTD) and multi-core (MC) for bottom water, and a long piston core (LC) for sediment and porewater (Curry et al. 2008). Porewater was extracted from core subsamples at 60 cm intervals with hydraulically driven titanium squeezers (modified after Manheim et al. (1974)).

Cores used for paleosalinity analysis were collected from 5 sites in the western North Atlantic (*Figure 2.2*) spanning 20 ° latitude (14.4 to 35.7 °N), 7 ° longitude (50.6 to 57.6 ° W), and 4453 to 5557 m water depth (*Table 2.1*). Including both abyssal plane and continental rise, these sites were selected to be advection free and span the likely LGM interface between northern and southern deep water cells. Sediment

thickness ranged from 98 to 1012 m (Divins 2003) overlaying 40 – 102 Ma basement (Müller et al. 2008). Sediment is nannofossil clay with pelagic red clay, containing up to 50 % foraminifera, 30 % siliceous ooze, 25 % silt turbidites, and 5 % radiolarian chert or diatom nannofossil ooze. Core penetration ranged from 26.8 to 40.2 meters below sea floor (mbsf).

Analyses

Porewater and bulk sediment densities, titration-determined $[Cl^-]$, SO_4^{-2}/Cl^- ratio, alkalinity (ALK), pH, dissolved inorganic carbon (DIC), and formation factor were measured onboard (data doi: 10.26022/IEDA/111472). Analyses performed after the expedition include cation concentrations (Mg^{+2}, Ca^{+2}, K^+), and titration-determined $[Cl^-]$ from Site 15 & 16.

Porewater Geochemistry

Porewater density was measured with the Anton Paar DM 5000 M using Milli-Q deionized water (DI) for calibration and International Association for the Physical Sciences of the Oceans (IAPSO) P156 seawater standard (Millero et al. 2008) as a quality check. We determined Cl^- by $AgNO_3$ titration of 1 cm^3 of the pore fluid, weighed for increased precision on titrations performed post-expedition, using a Metrohm 794 Basic Titrino autotitrator and Metrohm Ag Triode calibrated against IAPSO batch P156. Major ions were measured by ion chromatography as peak areas using a Metrohm 861 Advanced Compact Ion Chromatograph (IC). A large batch of diluted IAPSO was used as a working standard, while samples and quality check IAPSO standards were individually pipetted. Drift corrections were applied where necessary,

and sulfate was reported directly as a ratio of its peak area to that of chloride (SO_4^{-2}/Cl^-) while cation concentrations were calculated from their individual peak areas ratioed to the standard. ALK was determined by HCl Gran titration (Edmond 1970) using a Metrohm 809 Titrando autotitrator, calibrated against Dickson CRM seawater standard (Marine Physical Laboratory, Scripps Institution of Oceanography, Batch 156, certified ALK 2232.58 ± 29 µmol/kg, DIC 2040.94± 0.41µmolkg). Porewater was stripped of CO_2 and acidified to extract DIC, measured as CO_2 with a Marianda AIRICA™ and LICOR LI-7000 CO2/H2O infra-red analyzer. Carbonate equilibrium was used to calculate porewater bicarbonate concentration, *[HCO$_3^-$]*, from ALK and DIC after Edmond and Gieskes (1970).

Physical Properties

Diffusion along a complex path is assessed with porosity, ϕ, and tortuosity, ϑ^2, evaluated in our sediment cores using the formation factor, *f*, and densities of porewater and sediment. We measured *f* by Metrohm/Brinkman Conductometer with a home-built double electrode inserted into the center of freshly recovered, wet cores (McDuff et al. 1978) . Formation factor *f* the ratio of measured conductivities of reference bottom water to wet sediment, is used to calculated tortuosity ($\theta^2 = f\phi$),.

Uncertainty

Porewater geochemical profiles are expected to be smooth as a result of diffusion and the deviation from smoothness can be used to estimate total method error, sampling plus analytical. To account for error introduced by sampling and analysis, measured data was smoothed with a robust weighted local regression

(rLoess, (Cleveland and Devlin 1988)). Individual measurements differing from their smoothed values by greater than twice the profile's standard deviation are excluded. Uncertainty was determined for each measured property with a Monte Carlo technique by generating 100 random values at each measured depth (normal distribution, centered on smoothed value with a 90% range of twice the profile's standard deviation determined above). Averages and standard deviations of the Monte Carlo values at each depth are used for subsequent calculations and included as error bars (*Figure 2.3*).

Major ion concentrations of non-conservative solutes are ratioed to smoothed [Cl⁻] (R) and referenced to standard seawater composition at each site's bottom water salinity (ΔR_i) to account for diagenetic change.

Chloride from Porewater Density

In the approach of Homola et al. (Dissertation Chapter 1 2019), [Cl⁻] is calculated from the unsmoothed measured density and the smoothed relative solute ratios, ΔR_i, with equation 2.1 (see *Table 2.2* for symbol definitions), based on the equation of state for standard seawater (Millero et al. 2008) and accounting for the effects of diagenesis.

$$[Cl^-] = \frac{\rho_{meas} - \rho_{H_2O}}{a + \sum_i \Delta R_i Ar_i - \rho_{H_2O} \sum_i \Delta R_i V_i} \qquad (2.1)$$

Density determined [Cl⁻] is calculated at each depth (below the seafloor, bsf) for which porewater density and major ion concentrations (for each solute *i*) were measured. Smoothed measured densities are converted to [Cl⁻] using the equation of state for

standard seawater, without diagenetic corrections, to determine initial porewater [Cl⁻]

independent of higher uncertainty titration determined [Cl⁻]. This initial porewater [Cl⁻] is used to calculate relative solute ratios used in equation 2.1 to determined [Cl⁻]

from density. Equation 2.1 is then iterated with density determined chloride and ΔR_i

used to calculate each other until neither varies upon iteration. Please see Homola et

al. (Dissertation Chapter 1 2019) for details of this method.

LGM Bottom Water Salinity Reconstruction

To determine past bottom water chloride, we quantify the diffusive smoothing

porewater [Cl⁻] has experienced over time t through one-dimensional modeling of [Cl⁻]

diffusion in z (Eq. 2.2, see *Table 2.2* for symbol definitions)(Adkins et al. 2002; Insua et

al. 2014).

$$\phi \frac{\partial [Cl^-]}{\partial t} = \frac{\partial}{\partial z} \left(\frac{D}{f} \frac{\partial [Cl^-]}{\partial z} \right) \tag{2.2}$$

The Siddall et al. (2008) sea level curve, extending from the modern (pre-

industrial) to 70 ka, is scaled to represent bottom water [Cl⁻]. This boundary condition

(salinity as a function of time) is optimized until modeled porewater [Cl⁻] (Eq. 2.3) best

fits measured [Cl⁻] (minimum of the summed squared differences). [Cl⁻] is converted to

salinity, S, with equation 3 (see *Table 2.2* for symbol definitions) using the measured

bottom water density at each site (Lewis and Perkin 1978; Mcdougall et al. 2009;

Millero et al. 2008).

$$S = 1.80655[Cl^-] \frac{Ar_{Cl^-}}{\rho_{BW}} \tag{2.3}$$

LGM bottom water at each site is identified as the maximum in the best fit modeled porewater [Cl$^-$]. LGM bottom water salinity is determined as the corresponding maximum in optimized boundary condition salinity.

Results

The [Cl$^-$] profiles measured by density or titration for each site are shown in *Figure 2.3* with modeled best fits included. Salinity values for modern and LGM bottom water are listed in *Table 2.1*. Bottom water salinities associated with the peaks of these best fits, corresponding to the LGM, are shown along with modern S_{bw} as a function of latitude in *Figure 2.4*. Shallowest porewater salinities, from smoothed measured values, were within 0.3 % of the nearest WOCE bottom water salinities (Koltermann, Gouretski, and Jancke 2011) and differ between methods (titration vs. density) by less than 0.1 %.

Bottom water salinity change ΔS_{bw} between the modern and LGM ranges from 1.072 to 1.272 ± 0.005 g/kg when determined by density, a 3.07 to 3.65 ± 0.05 % change relative to LGM salinity. ΔS_{bw} ranges from 0.678 to 1.725 ± 0.02 g/kg when determined by titration, a 1.96 to 5.03 ± 0.09 % change relative to LGM salinity. While ΔS_{bw} is near constant for all sites, the absolute value of S_{bw} increases by 1 ± 0.2 % g/kg at sites 15 & 16 relative to the four southern sites, though both were measured post-expedition and have a higher uncertainty relative to sites where the density method (Eq. 1) could be applied. Chloride titration performed post-expedition represents an upper bound for porewater [Cl$^-$] because evaporation during storage imparts a consistent offset towards slightly higher [Cl$^-$] (Adkins and Schrag 2003; Homola

Dissertation 2019, Chapter 1). All six model fits have LGM peaks located deeper than collected samples (*Table 2.1*), adding uncertainty to LGM paleosalinity results, especially for titrated profiles where error associated with sample storage or pipetting increases uncertainty.

Discussion

We more than double the number of Atlantic sites where LGM bottom water salinity has been inferred from measured subseafloor data, with four sites quantified using our higher precision porewater density method. Density determined bottom water salinity for the modern and LGM is consistent across sites with an average value of 3.39 % salinity change between the modern and LGM very similar to the global average expected from sea level change (3.6 ± 0.3 %). Paleosalinities determined from 30 m density profiles collected during expedition KN223 have similar precision to Adkins, McIntyre, and Schrag's (2002) paleosalinities determined from 100 m chloride profiles by titration that capture the porewater chloride maximum associated with increased LGM salinity. High variation in titration determined salinity results can be reduced in profiles with low sample resolution or high analytical uncertainty if the LGM porewater chloride peak is sampled. Applying our density technique to samples collected through the LGM porewater chloride peak has the potential to yield bottom water paleosalinities with unprecedented precision.

Salinity change determined using our density method is consistent with water mass distribution changes based on published paleosalinity and benthic foraminiferal δ^{13}C, Δ^{14}C, and δ^{18}O data (*Figure 2.1*): during the LGM, northern deep water shoaled

51

during the LGM, while the southern circulation cell expanded northward. Sites 11 & 12 have oxygen present to basement and were analyzed for paleo-preformed nitrate (PFN) by Homola et al. (Homola et al. 2015), increasing by 6 and 4 µM respectively between the modern and LGM. Supported by the PFN and salinity change observed at KN223 sites, expansion of southern deep water during the LGM can account for two thirds of observed atmospheric CO_2 decrease during the LGM .

Adkins, McIntyre, and Schrag (2002) inferred a 2.7 − 6.9 ± 0.03 - 0.17 % salinity increase from the pre-industrial to the LGM, using chloride measured by titration and a similar model. Their three Atlantic paleosalinity sites, supported by subsequent studies, have been used to describe a deep Atlantic meridional salinity gradient reversal during the LGM. Our higher accuracy density-determined North Atlantic salinity results are consistent with this reversal, but differ in absolute value (*Figure 2.4*). All our western North Atlantic sites have an average salinity of 36.00 ± 0.09 g/kg, consistent with Galbraith and Lavergne (2019) and a full g/kg lower than Adkins, McIntyre, and Schrag (2002) determine by titration at 50 ^{o}S. We determine the relative average global salinity change from the modern to LGM in three different ways: i. 3.6 ± 0.3 % using sea level change; ii. 4.7 ± 0.1 % from chloride-determined paleosalinity measurements of Adkins, McIntyre, and Schrag (2002);and iii. 3.9 ± 0.1 % from Galbraith and Lavergne (2019) model results which are validated by our density-determined paleosalinity measurements. These percent changes in global salinity are rough estimates calculated from paleosalinity measurements and literature water mass distributions. We use a constant seawater density, a volume for the deep Pacific

twice the volume of the deep Atlantic, Pacific deep water composed of 10 % southern

sourced water, and Atlantic deep water composed of 80 % southern sourced water.

Paleosalinities measured in the north and south Atlantic and Pacific oceans are used

as the LGM salinities of their respective MOC cells (e.g. the southern Atlantic MOC

cell's LGM salinity is set to paleosalinity measured at 60 °S).

The four sites examined in this study constrain LGM Atlantic deep water

salinities for a region of mixing between northern and southern cells. Improved

latitude and depth resolution of paleosalinity data, especially in regions of deep water

formation and mixing between northern and southern sourced deep waters, remains

necessary to confirm the potential presence of northern abyssal water(Keigwin and

Swift 2017) and to further constrain the northward extent of the southern cell and the

depth to which the northern cell shoaled during the LGM. Porewater samples

collected from paleosalinity-relevant sites can be analyzed shipboard with the density-

based method, yielding higher precision than previously available techniques even

from lower-resolution sample profiles.

Conclusions

We determine bottom water salinity during the LGM at six sites in the western

North Atlantic, quantifying four using our high-precision density method. Porewater

[Cl$^-$] is measured by chloride titration and determined from measured density and

major ion concentrations. Measured porewater profiles are fit with a diffusion model

of bottom water salinity over time (scaled from sea level change) to determine LGM

bottom water salinities similar to those of nearby published sites. Bottom water

salinity change between the modern and LGM, relative to LGM salinity, ranges from

3.07 – 3.65 ± 0.05 % when determined by density, and from 1.96 – 5.03 ± 0.09 %

when determined by titration, consistent with global sea level informed salinity

change. We demonstrate the northward expansion of southern deep water and the

shoaling of northern deep water during the LGM based on salinities at previously

unsampled western North Atlantic sites measured using our high-precision density-

based method. Although the LGM paleosalinities we determined by density

measurement are lower than published paleosalinities determined by titration, our

results still support that there was a reversal of the Atlantic's north-south deep water

salinity gradient during the LGM.

Tables

Table 2.1. Atlantic Ocean sites where LGM bottom water salinity has been measured, in this study (KN223) or by Adkins, McIntyre, and Schrag (2002) (ODP). Salinities for present day, *S(0,0)*, from smoothed measured [Cl⁻]; LGM, *S(0,-21.7ka)*, from the diffusion model boundary condition; and their relative difference *ΔS$_{bw}$* are shown from the density and titration methods. Depth below seafloor of the porewater [Cl⁻] maximum from the model best fit, corresponding to the LGM bottom water salinity maximum, is shown for each profile.
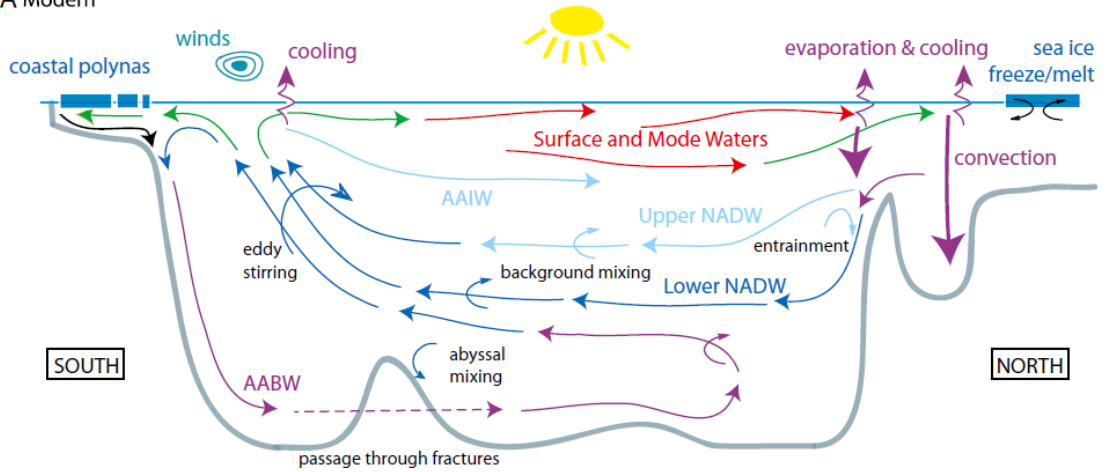
Study		KN223						ODP		
Site		3	10	11	12	15	16	1063	981	1093
Latitude (°N)		14.401		22.785	29.677	33.484	35.710	33.686	55.477	-49.976
Longitude (°E)		-50.623		-56.518	-58.328	-54.166	-57.615	-57.615	-14.651	5.866
Water Depth (m)		4453		5557	5367	5515	4575	4584	2184	3626
Density	*S(0,0)* (g/kg)	34.886 ± 0.019	34.844 ± 0.019	34.77 ± 0.023	34.794 ± 0.026					
	S(0,-21.7ka) (g/kg)	35.957 ± 0.012	36.116 ± 0.021	35.909 ± 0.027	36.038 ± 0.013					
	ΔS$_{bw}$ (%)	3.07 ± 0.03	3.65 ± 0.06	3.28 ± 0.08	3.58 ± 0.04					
	z(max [Cl⁻]) (mbsf)	35.5	36.5	34.5	35.5					
Titration	*S(0,0)* (g/kg)	34.74 ± 0.03	34.66 ± 0.06	34.44 ± 0.04	34.26 ± 0.08	35.79 ± 0.11	35.93 ± 0.05	34.885 ± 0.005	34.945 ± 0.008	34.685 ± 0.003
	S(0,-21.7ka) (g/kg)	35.77 ± 35.77	35.34 ± 35.34	35.49 ± 35.49	35.99 ± 35.99	37.18 ± 37.18	37.17 ± 37.17	35.83 ± 35.83	36.1 ± 36.1	37.08 ± 37.08
	ΔS$_{bw}$ (%)	2.96 ± 0.1	1.96 ± 0.21	3.04 ± 0.23	5.03 ± 0.19	3.89 ± 0.39	3.44 ± 0.14	2.7 ± 0.1	3.3 ± 0.3	6.9 ± 0.5
	z(max [Cl⁻]) (mbsf)	35.5	38.5	35.0	34.5	35.5	36.5	38	25	57
Sediment Thickness (m)		100		100	98	331	1012			
Sediment Density (kg/m³)		2656		2659	2661	2664	2667			
Core Penetration (mbsf)		28.7	33.9	28.2	28.8	26.8	40.2			
Site		3	10	11	12	15	16	1063	981	1093

55

Table 2.2. Index of variables, superscripts, and subscripts used in this paper.

Type	Symbol	Description	Unit
Variables	ρ_{meas}	Density, Measured	kg/m^3
	m	Mass	kg
	v	Volume	m^3
	Ar	Molecular Mass	kg/mol
	V	Partial Molar Volume	m^3/mol
	$[\,]$	Concentration	mol/L
	R	Ratio of Bottom Water Concentration to [Cl$^-$]	-
	ρ_{H2O}	Density of Pure Water	kg/m^3
	a	Slope of [Cl$^-$] vs. Density for Standard Seawater	mol/kg
	S	Salinity	g/kg
	ϕ	Porosity	%
	f	Formation Factor	-
	D	Free Solution Cl$^-$ Diffusion Coefficient	m^2/sec
	z	Depth	mbsf
	t	Time	sec
	ε	Propagated Error	varies
	σ	Measurement Error	varies
	Δ, δ	Difference	varies
	∂	Partial Derivative	varies
Subscripts & Superscripts	i	Solute Index	
	j	Depth Index	
	$meas$	Measured	
	BW, PW	Bottom Water, Porewater	
	o	Initial	

Figures

Figure 2.1. MOC schematic from Matsumoto (2017), showing a latitudinal cross section of the Atlantic Ocean during the modern (panel A) and LGM (panel B). Northern (NADW, AAIW; GNAIW) and southern (AABW, GSSW) cells are distinguished with blue and purple arrows respectively. Orange arrows show Keigwin and Swift's (2017) LGM northern abyssal water.
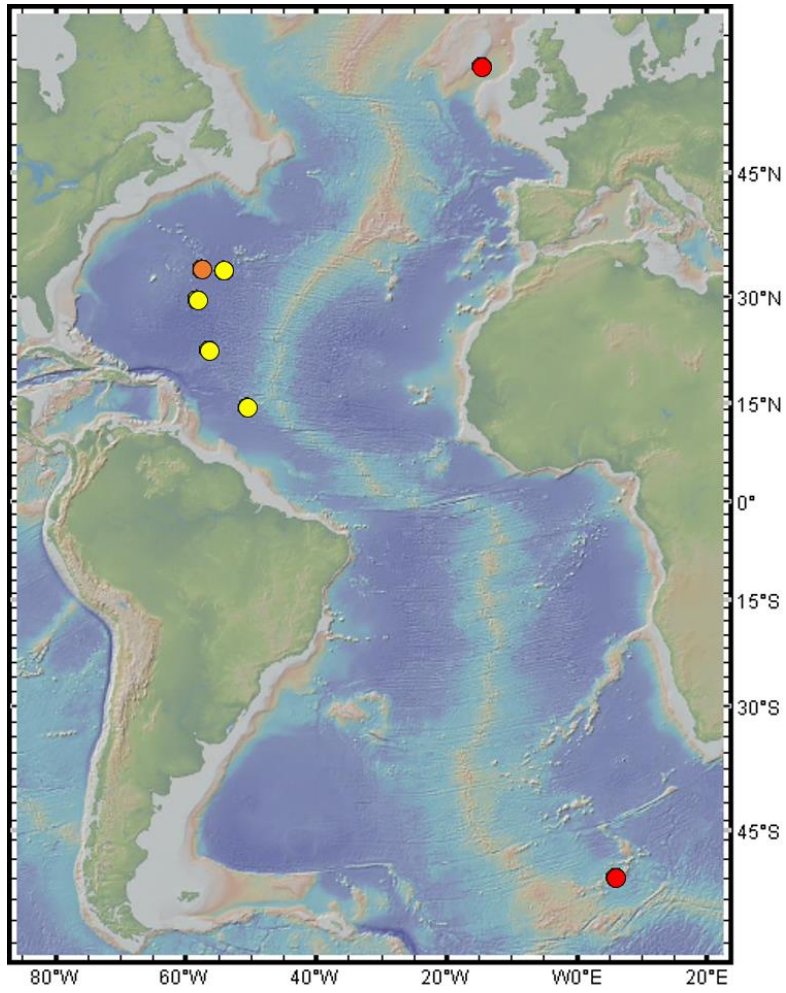
Figure 2.2. Locations of paleosalinity data from this study (KN223, yellow dots) and published Atlantic sites (Ocean Drilling Project, red dots) from Adkins, McIntyre, and Schrag (2002). Sites included in both studies are indicated in orange.

Figure 2.3. KN223 porewater salinity profiles measured by density (red) or titration (blue) from each site (number on panel). Measured profiles (x's) and their smoothed error (error bars) are shown with their diffusion model best fits (gray lines). All x-axes span 1.25 g/kg salinity, though bottom panels begin 1 g/kg saltier than those above.
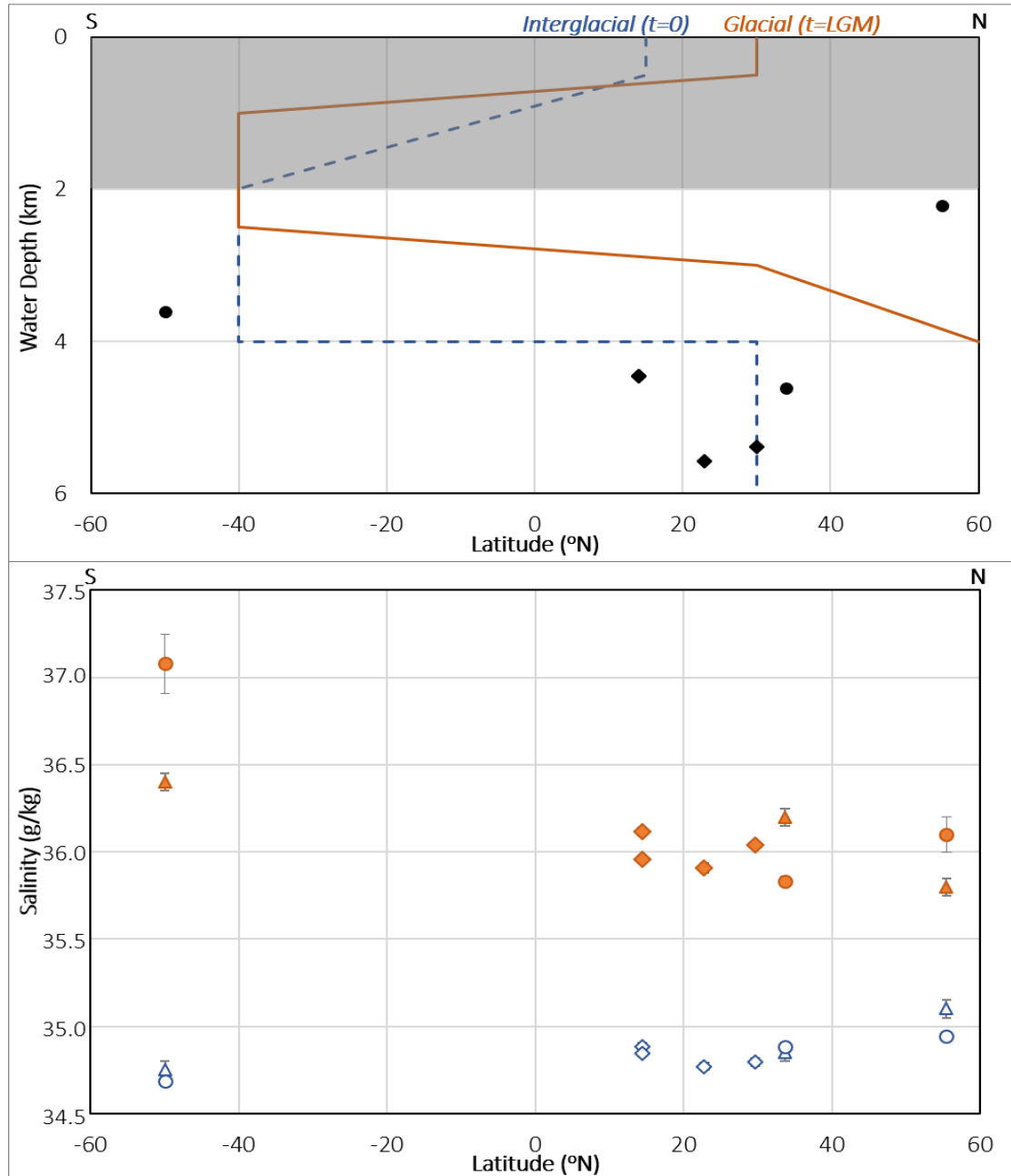
Figure 2.4. Atlantic water mass distribution (top) and bottom water salinity (bottom) of the modern (blue) and reconstructed LGM (orange). Representative boundaries between northern and southern deep water masses for t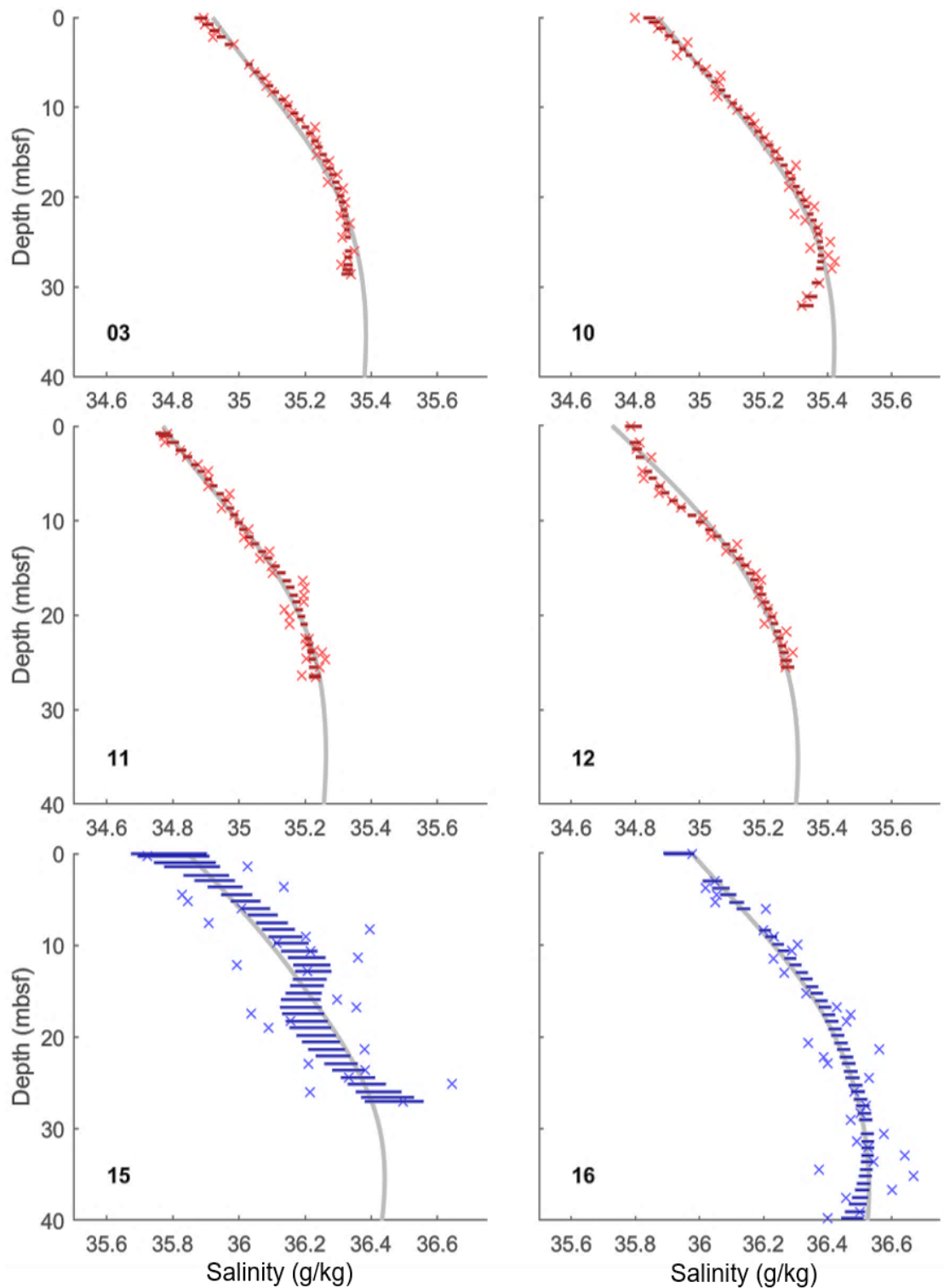he LGM (solid orange) and modern (dashed blue) determined from published LGM reconstructions (Adkins et al. 2005; Burke et al. 2015; Curry and Oppo 2005; Galbraith and Lavergne 2019; Insua et al. 2014; Lund et al. 2011; Lynch-Stieglitz et al. 2007). Atlantic paleosalinity sites are included on the top panel in black, distinguishing KN223 (diamonds) from published (circles) sites. Bottom water salinity values for the modern (open blue) and LGM (solid orange) are shown in the bottom panel: including results from the KN223 expedition (diamonds); Galbraith and Lavergne (2019)(triangles); and Adkins, McIntyre, and Schrag (2002)(circles). Bottom waters are distinguished from surface waters at 2 km water depth: above 2 km (gray shading top panel), salinities differ from bottom water values at all latitudes without deep water formation.

MANUSCRIPT 3

Nitrogen Abundance and Isotopic Composition of Subducting Deep Subseafloor Sediment and Porewater at Site IODP-C0023

by

Kira Homola[1], Florence Schubotz[2], Rebecca Robinson[1], Arthur J. Spivack[1],

Chawalit Charoenpong[3], Scott Wankel[3]

[1]University of Rhode Island Graduate School of Oceanography
[2]MARUM Center for Marine Environmental Sciences, University of Bremen
[3]Woods Hole Oceanographic Institution

Abstract

We investigate nitrogen concentrations and isotopes in the solid and dissolved phases of subducting seafloor under conditions that approach the canonical temperature limit of life. Nitrogen isotopic composition profiles of deeply buried porewater dissolved reduced nitrogen (ammonium, amino acids, etc.) are a first-of-their-kind dataset that we combine with a broad range of measured physicochemical properties to distinguish between biotic and abiotic nitrogen reactions. Porewater NH_4^+ ranges from 10 mol/kg at 200 mbsf to 0.1 mol/kg near basement, and the difference in nitrogen isotopic composition between porewater dissolved reduced nitrogen and sediment total nitrogen ranges from 0 to 4.7 ‰ with minimum sediment $\delta^{15}N$ of 1.3 ‰ and porewater $\delta^{15}N$ of 2.56 ‰. We assign these large isotopic variations to a variety of microbially mediated diagenetic processes including assimilation, ammonification, sulfate reducing ammonia oxidation, accretion, dissolution, and illitization.

<u>Introduction & Background</u>

Nitrogen is a highly reactive element that cycles through Earth's atmosphere, lithosphere, biosphere, and ocean. Essential to life, N plays a critical role in microbial metabolism as an electron donor and acceptor (e.g., D'Hondt et al. 2019; Holm and Neubeck 2009; Stüeken et al. 2016). Surface ocean primary producers convert dissolved inorganic N (N_2, N_2O, NH_4^+, NO_3^-, NO_2^-) to organic N (including amino acids, proteins, and nucleic acids), a fraction of which is vertically transported and collects as sediment on the underlying oceanic basement rock (for review see, Holloway and Dahlgren 2002). A link between surface and deep Earth reservoirs, subducting oceanic lithosphere transfers N into Earth's mantle, potentially impacting the abundance and isotopic composition of N returned to the atmosphere through melting and degassing at subduction zones and mid-ocean ridges (Halama et al. 2014) and altering Earth's atmospheric chemistry on geologic timescales (Berner 2006). The abundance and isotopic composition of subseafloor N species provide key insights into sediment diagenesis, past and present redox regimes, microbial metabolism, and sedimentary rock metamorphism (Jørgensen and Marshall 2016; Mallik, Li, and Wiedenbeck 2018; Zerkle and Mikhail 2017).

Home to as many microbial cells as the global ocean, the subseafloor accommodates a significant fraction of Earth's total living biomass (Kallmeyer et al. 2012; Parkes et al. 2014). Understanding the transformations that N undergoes in this complex environment requires examining the dissolved and mineral-bound, inorganic and organic N reservoirs deep below the seafloor. Here, dissolved N is present in the

forms of N_2, N_2O, NH_4^+, and dissolved organic N (DON, e.g. amino acids). Aqueous phase NH_4^+ and DON are collectively referred to as dissolved reduced N (DRN) in this study. Solid phase, sediment N (TN) includes organic material (TON) and NH_4^+ bound to minerals.

Nitrogen reactions in the deep subseafloor (*Figure 3.1*) include those potentially occurring in the chemically and thermally diverse, anoxic environment from 100 meters below seafloor (mbsf) to basement. Reduced N in sedimentary porewaters occurs as a results of metabolic processes; abiotic reactions, including dissolution of organic matter (OM) and desorption (Hoch et al. 1996; Williams et al. 1995); or transport, diffusion and advection (Holloway and Dahlgren 2002; Li, Bebout, and Idleman 2007). Enrichment or depletion of DRN in porewater can be microbially mediated through several pathways. NH_4^+ specifically may be involved in both anabolic and catabolic microbial reactions, such as the assimilation of NH_4^+ into cells or the oxidation of NH_4^+ by sulfate (known as sulfate reducing ammonium oxidation (SRAO)(Schrum et al. 2009). Abiotic removal of NH_4^+ occurs during illitization through the incorporation of NH_4^+ into illite's sheet structure, observed under the microbial, temperature, and pressure regimes of the deep subseafloor (Schroeder and McLain 1998; Williams et al. 1995; Yang et al. 2016). Remineralization of TON and the release of NH_4^+ over geologic timescales can promote N sorption by minerals that in turn metamorphose under high pressure and temperature. Subduction of N-enriched sediment increases the primary input of surface N into the deep Earth (Busigny, Cartigny, and Philippot 2011; Mallik et al. 2018) and influences its isotopic

composition upon return to the atmosphere (e.g. Haendel et al. 1986; Labidi et al. 2020).

Vertical isotopic profiles in sediment provide further insight into which mechanisms control porewater NH_4^+ distributions because changes in the isotopic signature of each compound can reflect fractionations associated with different transfer pathways (Stüeken et al. 2016). Known fractionations for potential reaction pathways are included in *Table 3.1*. NH_4^+ assimilation is thought to preferentially remove ^{14}N from the porewater (Hoch, Fogel, and Kirchman 1992; Lehmann et al. 2002; Prokopenko et al. 2004). Abiotic uptake through cation exchange and/or illitization (Charlesworth 1986; Koo et al. 2014; Schroeder and McLain 1998; Williams et al. 1995) negligibly fractionates or preferentially removes heavier ^{15}N (Sadofsky and Bebout 2000). We examine N distribution, speciation, and isotopic composition in subducting deep subseafloor porewater and sediment to identify likely diagenetic reactions involving dissolved, sedimentary, and biological N (*Figure 3.1*, *Table 3.1*).

Materials and Methods

Site Description & Sample Acquisition

International Ocean Discovery Program (IODP) Expedition 370 (doi: 10.14379/iodp.proc.370.2017) was designed to comprehensively study the biomass, activity, metabolism, and diversity of microbial communities in a subseafloor environment selected to encompass the likely biotic-abiotic transition zone (Heuer et al. 2017). Site C0023 (32°22.00′N, 134°57.98′E) was drilled within the Shikoku Basin of the Nankai Trough protothrust zone (*Figure 3.2*) in 4776 m of water. Downhole,

temperatures increase through the accretionary prism and subducting formation from ~2°C at the seafloor to ~120°C at the sediment/basement interface 1180 mbsf (Heuer et al. 2017; Hinrichs et al. 2016). Porewater was extracted by hydraulic press (Manheim 1974) from 5 to 10 cm whole round core samples scraped of any potential drill fluid contaminated material in a near-anoxic glove bag. Porewater samples collected for post-expedition N analysis were frozen at -80°C. The topmost 189 mbsf of sandy-turbidite dominated sediment was not collected at Site C0023. Instead, data from nearby Site 1174 (32°20.5′N, 134°57.4′E) is used to inform lithology and dissolved NH_4^+ in the upper 200 mbsf (Moore et al. 2001). Dissolved NO_3^- or NO_2^- and their reactions, including annamox, are not considered because the sediment column is anoxic; porewater oxygen is depleted within a meter of the seafloor (Inagaki et al. 2019).

Lithology

At Site C0023 turbidite and ash-rich trench-dominated facies (Upper Shikoku) overlie volcaniclastic basin and terrestrial-dominated organic matter hemipelagic sediments (Lower Shikoku) (Hinrichs et al. 2016). The Upper/Lower Shikoku basin transition reflects a change in sedimentation rate from very rapid deposition, with 635 m of sediment deposited in 0.4 Ma, to slower accumulation, 485 m deposited from 12.5 to 0.4 Ma at depth (Wen, 2018). Samples from 189 – 494 mbsf, reflecting a temperature range of 30 – 60 °C, were from sandy turbidites with 40-65 wt.% clay minerals. Samples from 494 – 635 mbsf, 60 – 72 °C, are clays (65-75 wt.%) composed of 80% smectite with minimal detrital illite (Kim et al. 2019). Samples from the Lower

Shikoku, 635 – 796 mbsf, are volcaniclastic mud with up to 10 wt.% illite. The sampling

transitions through the highly-fractured décollement zone (758-796 mbsf). Below the

décollement, 796 - 1180 mbsf and 86 - 120 °C, samples are volcaniclastic mudstone

and over 75 wt.% clay. The transitions in lithology, sedimentation rate, and the

complex hydrothermal and geotectonic setting indicate a non-steady-state diffusion

environment.

Nitrogen Isotope Analyses

Post-expedition, we measured the N isotopic composition of porewater DRN

and sedimentary TN. N isotopic composition ($\delta^{15}N$) is reported in per mil (‰) and

referenced to air (equation 3.1).

$$\delta^{15}N = \left(\left(^{15}N/^{14}N\right)_{sample} / \left(^{15}N/^{14}N\right)_{sample} - 1 \right) 1000 \qquad (3.1)$$

We adapted the persulfate oxidation denitrifier method for DRN analysis of

deep porewater samples (Knapp, Sigman, and Lipschultz 2005). Persulfate oxidizing

reagent, POR, was mixed daily from 6 g of thrice-recrystallized potassium persulfate

($K_2S_2O_8$), 6 g of NaOH, and 100 mL of deionized water (DI). Two standards similar in

concentration to porewater DRN were used to confirm full oxidation of DRN to NO_3^-:

International Atomic Energy Agency (IAEA N2) ammonium sulfate ((NH_4)$_2SO_4$) and

Aminocaprioic Acid (ACA) 6-aminocaprioic acid, used as in-house standards. Samples

and standards were brought to room temperature, well mixed, and aliquoted to

achieve a target concentration of $20 - 60$ μM NO_3^- in the final 3 mL of POR. A

concentration series of 20, 40, 60, and 100 μM was generated for each of the

standards (IAEA N2 and ACA), again in 3 mL POR. After POR reagent addition vials

were sealed, well mixed, and heated under pressure for 30 minutes.

The concentration of DRN in each vial was determined by measuring the NO_3^-

present after oxidation by chemiluminescent detection after conversion to NO with

vanadyl sulfate using a NOx Box (Teledyne Chemiluminescence NO/NOx Analyzer

200E)(Braman and Hendrix 1989). Complete oxidation of DRN was confirmed for

batches of blanks and standards before any samples were oxidized. Between POR

oxidation and IRMS analysis, samples were stored frozen at -4 $^\circ$C.

The stable N isotopic composition of the DRN oxidized to NO_3^- using the

persulfate oxidation method was measured with the denitrifier method by gas

chromatograph and Thermo Delta V Advantage Isotope Ratio Mass Spectrometer (GC-

IRMS) with a custom build purge and trap system at URI (Knapp et al. 2005; Sigman et

al. 2001). High pH POR samples and standards were acidified to a pH of 3 ± 1 with

approximately 500 μL of 6 M HCl^- per vial. All $\delta^{15}N$ values were standardized using

IAEA N3 ($\delta^{15}N$ = 4.7 ‰) and United States Geologic Survey (USGS) 34 ($\delta^{15}N$ = -1.8 ‰).

Replicates from all batches are averaged to determine $\delta^{15}N$ of individual samples and

uncertainty is calculated as the standard deviation of all replicates (error bars in *Figure*

3.3).

We also evaluated the hypobromite method (Zhang et al. 2007) for measuring

dissolved N isotopes, which uses a hypobromite (BrO^-) reagent to convert all DRN to

NO_2^- before reduction to N_2O gas with a 1:1 sodium azide and acetic acid buffer

solution. Conversion of DRN to nitrite was evaluated from the difference between

[NH$_4^+$] measured shipboard and [NO$_2^-$] present after hypobromite oxidation. Despite oxidizing samples with more hypobromite reagent relative to sample than Zhang et al. (2007) used in seawater, full hypobromite oxidation of NH$_4^+$ was inhibited in porewater samples. This finding is consistent with other attempted application of the hypobromite method to methane seep and hydrothermal vent porewater samples, and conversion by hypobromite of several dissolved organics (Zhang et al. 2007 supplemental material). The high organic content of deep subseafloor porewaters (Heuer et al. 2017) likely inhibits quantifiable conversion of DRN by hypobromite reagent. We recommend N isotopes of complex, non-standard seawater samples be measured through the persulfate-denitrifier method.

Nitrogen isotopes of bulk solids, $\delta^{15}N_{TN}$, were measured following the approach of Sepúlveda et al. (2009), capturing both inorganic and organic $\delta^{15}N$ of the sediment. Prior to analysis samples were treated with HCl to remove inorganic carbon and oven-dried. Analysis was performed with a ThermoFinnigan Trace GC Ultra coupled to a MAT Delta Plus mass spectrometer via a GC Combustion III. Isotope values were corrected for air N$_2$ using IAEA ammonium salt (Werner and Brand 2001) and checked against internal lab standards.

Organic Nitrogen Abundance

[DON] is calculated by subtracting shipboard fluorescence-determined [NH$_4^+$]$_{aq}$ from persulfate-determined [DRN]. [TON] is estimated from [TOC] measured shipboard and a constant C:N ratio of 15:1, appropriate for anoxic organic matter (Schmidt et al. 2011). We calculate the fraction of organic N for porewater and

sediment, reported in percent (%), as [DON]/[DRN] and [TON]/[TN] using shipboard measurements of DRN and TN (Heuer et al. 2017; Morono et al. 2017).

Because the sums of inorganic and organic N are measured as bulk N of porewater and sediment, it is important to note that we did not directly measure differences in isotopic composition between inorganic and organic N or the abundance of organic N.

Results

Nitrogen Abundance and Distribution

At C0023, porewater DRN is predominantly NH_4^+ (65-100%), with measurable DON present deeper than 450 mbsf (*Figure 3.3*). TN including TON and mineral-associated NH_4^+ is approximately 1000 times as abundant per kg sediment as DRN. $\delta^{15}N_{TN}$ is consistently lighter than $\delta^{15}N_{DRN}$, converging at only two regions in the formation.

TON fractional abundance decreases linearly from 189 to 796 mbsf from 59 ± 6 to 32 ± 2 %, shifts to a constant value of 30 ± 3 % from 796 to 1000 mbsf, and experiences a stepwise increase to 37 ± 1 % at 1000 mbsf before decreasing approximately linearly to 16 ± 4 % at basement (*Figure 3.3*). As shown by Heuer et al. (2017), TN decreases approximately linearly from the shallowest collected sample to the base of the décollement (189 to 796 mbsf) from 9.5 ± 0.2 to 5.4 ± 0.3 mol_N/kg_{sed}. TN then shifts to a near constant value of 7.9 ± 0.6 mol/kg from 796 to 1102 mbsf before decreasing to 4.8 ± 0.2 mol/kg above basement (1180 mbsf).

DRN is composed of 100 ± 1 % NH_4^+ from 189 to 428 mbsf, where DON begins

to increase from 0 ± 1 % at 428 mbsf to 26 ± 6 % below the décollement, with high

variation in DON % from 600 to 796 mbsf (*Figure 3.3*). DON remains relatively constant

at approximately 29 ± 8 % from 796 to 1000 mbsf with a single measurement at 1075

mbsf of 73 %. DON error is dominated by uncertainty introduced during the oxidation

of DRN by POR, as shipboard [NH_4^+] was measured to a precision of 0.001 mmol/kg

(Heuer et al. 2017).

[NH_4^+] increases from below detection at the seafloor (Moore et al. 2001) to a

maximum of 10.3 mmol/kg at 200 mbsf (Heuer et al., 2017, excluded from *Figure 3.3*

to better display lower concentration trends), consistent with the [NH_4^+] porewater

maximum of over 12 mmol/kg at 175 mbsf at Site 1174 (Moore et al. 2001). C0023

[NH_4^+] decreases from 10.31 to 2.22 ± 0.07 mM with generally concave-up curvature

from 200 to 494 mbsf (Unit II), then shifts to 1.41 ± 0.01 mM before decreasing

monotonically to 0.38 ± 0.02 mM at the base of the décollement (796 mbsf). [NH_4^+] is

approximately constant at 0.32 ± 0.04 mM from 796 to 1032 mbsf before decreasing

to 0.20 ± 0.04 near basement. Two local maximums of 1.3 ± 0.2 mM and 1.1 ± 0.2 mM

occur at the Unit II/III boundary (637 mbsf) and above the décollement (739 mbsf)

respectively (*Figure 3.3*).

Nitrogen Isotopes

$\delta^{15}N_{TN}$ increases from 1.7 ± 0.2 to 2.9 ± 0.1 ‰ through Unit II (189 to 494

mbsf) except for a small decrease to 2.1 ± 0.3 ‰ in Unit IIC (459 mbsf)(*Figure 3.3*).

$\delta^{15}N_{TN}$ remains constant at 3.0 ± 0.3 ‰ through Unit III (494 to 637 mbsf) and

gradually shifts through the profile's minimum of 1.3 ± 0.1 ‰ at 688 mbsf to a

constant value of 2.1 ± 0.3 ‰ through Unit IV above the décollement (637 to 796

mbsf). Returning abruptly to 3.2 ± 0.1 ‰, $\delta^{15}N_{TN}$ remains constant from 796 to 1000

mbsf before decreasing to a local minimum of 2.2 ± 0.1 ‰ near basement (1124

mbsf).

$\delta^{15}N_{DRN}$ is nearly constant at 5.6 ± 0.1 ‰ from the shallowest measured

sample (304 mbsf) to 450 mbsf, 3.2 - 2.2 ± 0.1 ‰ higher than $\delta^{15}N_{TN}$ (*Figure 3.3*).

$\delta^{15}N_{DRN}$ then decreases monotonically to 3.2 ± 0.2 ‰, converging with $\delta^{15}N_{TN}$, by 535

mbsf and remains relatively constant until the Unit III/IV transition at 637 mbsf. An

abrupt shift occurs in $\delta^{15}N_{DRN}$ to the formation maximum of 6.5 ± 0.5 ‰ at 661 mbsf,

4.7 ‰ higher than $\delta^{15}N_{TN}$ at this depth (*Figure 3.3*, *Figure 3.4*). $\delta^{15}N_{DRN}$ decreases from

this maximum to 4.7 ± 0.1 ‰, where it remains constant from 703 to 796 mbsf,

consistently 2.6 ‰ higher than $\delta^{15}N_{TN}$. A single low value of 3.1 ± 0.2 ‰ at 825 mbsf,

approximately equal to the $\delta^{15}N_{TN}$ value, occurs below the décollement. Below this

point, $\delta^{15}N_{DRN}$ values are higher and decreasing from 5.4 ± 0.5 ‰ at 855 mbsf to

converge on 3.1 ± 0.4 ‰, again equal to the $\delta^{15}N_{TN}$ values, from 1015 to 1075 mbfs.

Discussion

To identify processes occurring at different depths in the C0023 formation, we

consider the addition or loss of N from measured pools (*Figure 3.1*) and any known

isotopic fractionations associated with these transformations. Differences in isotopic

composition between N reservoirs across specific pathways can be described in terms

of isotope enrichment effect ε, approximated for N in equation 3.2.

72

$$\varepsilon_N = \delta^{15}N_{product} - \delta^{15}N_{reactant} \qquad (3.2)$$

Isotope enrichment effects associated with pathways that have been assessed

through culture experiments, *in-situ* measurements, and modeling are included in

Table 3.1 and used to help identify likely C0023 N pathways.

While measured N concentration and isotopic profiles at C0023 are a first-of

their kind dataset and remain to be rigorously evaluated, a transition from biotic-

dominated reactions above 637 mbsf (Upper Shikoku) to thermogenic-dominated

reactions below the décollement (796 mbsf, 86°C) can explain the observed trends.

This shift in reaction regime with depth, temperature, and lithology is independently

identified by Heuer et al. (2020, in press) through cell count, spore abundance, carbon

composition, profiles of additional substrates, and isotopic tracer experiments. They

conclude that microbial activity varies as a function of both geological and

physiological factors but is still detectable in 120 °C sediments overlying ~16 ma

oceanic crust, supporting microbially-mediated uptake of DRN as the predominant

cause of observed $\delta^{15}N_{DRN}$ and $\delta^{15}N_{TN}$ differences.

NH_4^+ production from microbial organic matter remineralization

(ammonification) is likely occurring in the upper 200 mbsf and is likely the primary

source of porewater NH_4^+ (Arndt et al. 2013; Brandes and Devol 1997; Wehrmann et

al. 2011). Porewater NH_4^+ produced through ammonification is expected to have a

similar or slightly lower $\delta^{15}N$ value relative to its source organic matter (Macko et al.

1987; Prokopenko et al. 2004; Robinson et al. 2012). Through most of the C0023

profile, however, $\delta^{15}N_{DRN}$ is greater than $\delta^{15}N_{TN}$. Uptake and assimilation of NH_4^+, degradation of TON, or another process must be causing an increase in $\delta^{15}N_{DRN}$.

At nearby Site 1174, maximum porewater NH_4^+ (10 mM) occurs at 200 mbsf. This depth corresponds to the shallowest samples collected at C0023, with elevated $\delta^{15}N_{DRN}$ values relative to $\delta^{15}N_{TN}$ and the lowest $\delta^{13}C$ of TOC values measured at C0023 (Schubotz et al., unpublished data). Partial NH_4^+ assimilation by subseafloor microbes (ε = -4 to -27 ‰ Hoch et al. 1992) could explain the elevated $\delta^{15}N_{DRN}$ if the 10 mM peak we observe in NH_4^+ represents a net rather than a gross maximum in NH_4^+ production. DRN from 200 to 637 mbsf decreases in concentration as $\delta^{15}N_{DRN}$ decreases to converge with $\delta^{15}N_{TN}$ (*Figure 3.4*), consistent with preferential uptake of heavy DRN by microbes through assimilation, SRAO, or bio-mediated illitization. Methane in this interval has a biogenic source, identified from a ratio of $CH_4/(C_2H_6+C_3H_8)$ greater than 1000 (Bernard, Brooks, and Sackett 1976; Heuer et al. 2017), where values less than 100 indicate a thermogenic CH_4 source. Harris (2020) calculated free energy yields for anaerobic oxidation of methane (AOM) reactions coupled to SO_4^{-2}, NO_2^-, NO_3^{-2}, H^+, Mn(Iv), and Fe(III), finding that NO_2^- dependent AOM is the most energetically favorable reaction modeled. While anoxic sediments are not expected to maintain detectable concentrations of oxidized N, rapid production and subsequent consumption of oxic intermediates (e.g. NO_2^-) has been observed in anoxic water column and subseafloor environments (Buchwald et al. 2018; Casciotti 2016). The isotopic impact of such rapid turnover is generally assumed to be negligible.

Decreasing cells and spores through the region of low sulfate and abundant CH_4 (Heuer et al. 2017) are consistent with decreased microbial production and a corresponding decrease in uptake of porewater NH_4. The observed decrease in $\delta^{15}N_{DRN}$ with depth could occur if porewater $\delta^{15}N_{NH4+}$ is heavier than $\delta^{15}N_{DON}$ and/or heavier DRN is preferentially removed from porewater by a fractionating uptake reaction. In shallow anoxic sediments Prokopenko et al. (2006) explain similar isotopic offsets between porewater NH_4^+ and sediment TN through preferential decomposition of isotopically heavier, more labile marine organic matter over isotopically lighter, refractory terrestrial organic N (Prokopenko et al. 2004; Sweeney and Kaplan 1980). SRAO to NO_2^-, a reaction energetically favorable in shallow anoxic sediments when coupled to NO_2^- reducing ammonium oxidation (Schrum et al. 2009), could also be occurring at C0023 from 200 to 637 mbsf coupled to NO_2^- AOM, consistent with observed decreases in SO_4^{-2} and DRN concentrations.

The isotopic difference between dissolved and sediment N decreases from 494 to 550 mbsf, where $\delta^{15}N_{DRN}$ converges with $\delta^{15}N_{TN}$ and remains constant until the Upper/Lower Shikoku Basin transition (637 mbsf). Coincident $\delta^{15}N_{DRN}$ and $\delta^{15}N_{TN}$ could represent a region where dissolved NH_4^+ is produced through ammonification without fractionation or subsequent alteration/uptake. The overall loss of dissolved NH_4^+ observed through this interval could be due to weaker DRN production or subsequent consumption of DRN through non-fractionating microbially mediated accretion of DON to TON.

The porewater NH_4^+ concentration and $\delta^{15}N_{DRN}$ decrease observed between

the Upper/Lower Shikoku Basin boundary (637 mbsf) and the base of the décollement

(796 mbsf) is likely due to illitization, which consumes porewater NH_4^+ through its

increase in available cation bonding sites and preference for the higher ionic radius of

NH_4^+ over K^+ (Meunier, Lanson, and Beaufort 2000; Wilson 2002). Through this

interval, sediment composition shifts from 65 % clay composed of 80 % smectite with

minimal detrital illite to 75 % clay with up to 10 % bio-mediated illite, where microbial

uptake of smectite-bound-Fe(III) as an electron acceptor could promote illite

formation (Kim et al. 2019). The shallowest thermogenically-derived methane at

C0023 is observed at the Unit III/IV boundary (635 mbsf), supporting bio-dominated

pathways transitioning to include abiotic processes from 637 to the base of the

décollement. $\delta^{15}N_{TN}$ and $\delta^{15}N_{DRN}$ remain constant at 2.0 and 4.1 ± 0.1 ‰ from 650

mbsf to the base of the décollement, supporting a decrease in microbial activity

and/or predominantly non-fractionating reactions. [DRN], [TN], and $\delta^{15}N_{TN}$ remain

constant from the 796 to 1000 mbsf while $\delta^{15}N_{DRN}$ decreases by 2.3 ‰ to converge

with $\delta^{15}N_{TN}$ at 3.2 ‰. TN increases abruptly by 5 mol/kg below the décollement, TON

makes up only 30 % of TN, sediment changes to a more clay-dominated lithology, and

hydrothermal alteration increases with depth (Heuer et al. 2017). Diagenetic illite is

produced thermogenically throughout this interval, experiencing a number of

structural transitions with depth that consume increasing dissolved NH_4^+ relative to

overall clay mineral composition (Schroeder and McLain 1998). Schroeder and McLain

(1998) found that fixed nitrogen content in shales roughly doubled as the illite to

smectite ratio doubled. At C0023, illitization converts 20 % of the smectite present (Kim et al. 2019) and DON makes up 25 % of DRN, consistent with illitization coupled to thermogenic-driven dissolution of TON. Decreasing $\delta^{15}N_{DRN}$ (4.7 ‰ below-décollement to 3.2 ‰ above-basement, coincident with $\delta^{15}N_{TN}$) is consistent with uptake of porewater NH_4^+ into clay minerals if heavy N is preferentially incorporated or if porewater $\delta^{15}N_{NH4+}$ is heavier than $\delta^{15}N_{DON}$.

Conclusions

We present the first coupled N porewater concentration and isotope dataset from deep subseafloor sediments, collected from 200 mbsf to basement at IODP Site C0023. Potential N processes occurring over the observed range of temperatures and lithologies are identified by coupling our data with clay mineral abundance; inorganic and organic C; and sulfur of solid and dissolved phase samples. Dissolved NH_4^+ ranges from 10mmol/kg at 200 mbsf to 0.1 mmol/kg near basement, and the difference in $\delta^{15}N$ between porewater and sediment ranges from 0 to 4.7 ‰. Likely biogeochemical regimes transition from highly microbially mediated above 637 mbsf, through production of dissolved NH_4^+ by ammonification and subsequent microbial uptake, transitioning to thermogenically dominated below the décollement at 796 mbsf, through illitization of a different organic matter source. Insights on the biogeochemical cycling of NH_4^+ and DRN from the Nankai subduction zone may be extended to similar temperature, lithology, and chemical regimes in large regions of the global subseafloor.

Tables

Table 3.1. Potential pathways involved in anoxic subseafloor nitrogen cycling, color-coded by association: bio-mediated in green, thermogenic in orange, either in blue. Abbreviations are provided where appropriate. Representative net reactions from Stüeken et al. (2016) are listed. Pathways resulting in the addition (+) or loss (-) of inorganic (NH_4^+) or organic (DON) nitrogen to porewater or sediment nitrogen reservoirs are indicated where applicable. The nitrogen isotope fractionation, ε_N, associated with each pathway is included if available (referenced in the far-right column).

Pathway	Reaction (net)	Porewater Δ		Sediment Δ		ε_N (‰)	Reference
		NH4+	DON	NH4+	TON		
N$_2$ Fixation	$N_2 + 6e^- + 8H^+ \rightarrow 2NH_4^+ \rightarrow (org \cdot NH_2)_{aq}$	+ / −	+			-8 : +1	Zhang et al. 2014
Ammonification	$(org \cdot NH_2)_{aq} + 2H^+ \rightarrow NH_4^+$	+	−			0	Prokopenko et al. 2004
Ammonium Assimilation	$NH_4^+ \rightarrow (org \cdot NH_2)_{aq} + 2H^+$	−	+			-4 : -27	Hoch et al. 1992
Sulfate Reducing Ammonium Oxidation (SRAO)	$8NH_4^+ + 3SO_4^{-2} \rightarrow 4N_2 + 3HS^- + 12H_2O + 5H^+$	−					
	$4NH_4^+ + 4SO_4^{-2} + 5CH_2O \rightarrow 5CO_2 + 2N_2 + 11H_2O + 4HS^-$	−					
Bio-Mediated Accretion	$(org \cdot NH_2)_{aq} \rightarrow (org \cdot NH_2)_s$		−		+		
Bio-Mediated Dissolution	$(org \cdot NH_2)_s \rightarrow (org \cdot NH_2)_{aq}$		+		−		
Cation Release	$(clay \cdot NH_4) \rightarrow clay + (NH_4^+)_{aq}$	+		−			
Cation Sorption	$clay + (NH_4^+)_{aq} \rightarrow (clay \cdot NH_4)$	−		+			
Illitization	$smectite + (NH_4^+)_{aq} \rightarrow (illite \cdot NH_4)$	−		+			
Abiotic Dissolution	$(org - NH_2)_s \rightarrow (NH_4^+)_{aq}$	+			-		
Metamorphism	$(clay - NH_4) \rightarrow (N_2, N_2O)_{aq}$			-			
Gas Exchange	$(N_2, N_2O)_{aq} \leftrightarrow (N_2, N_2O)_g$						
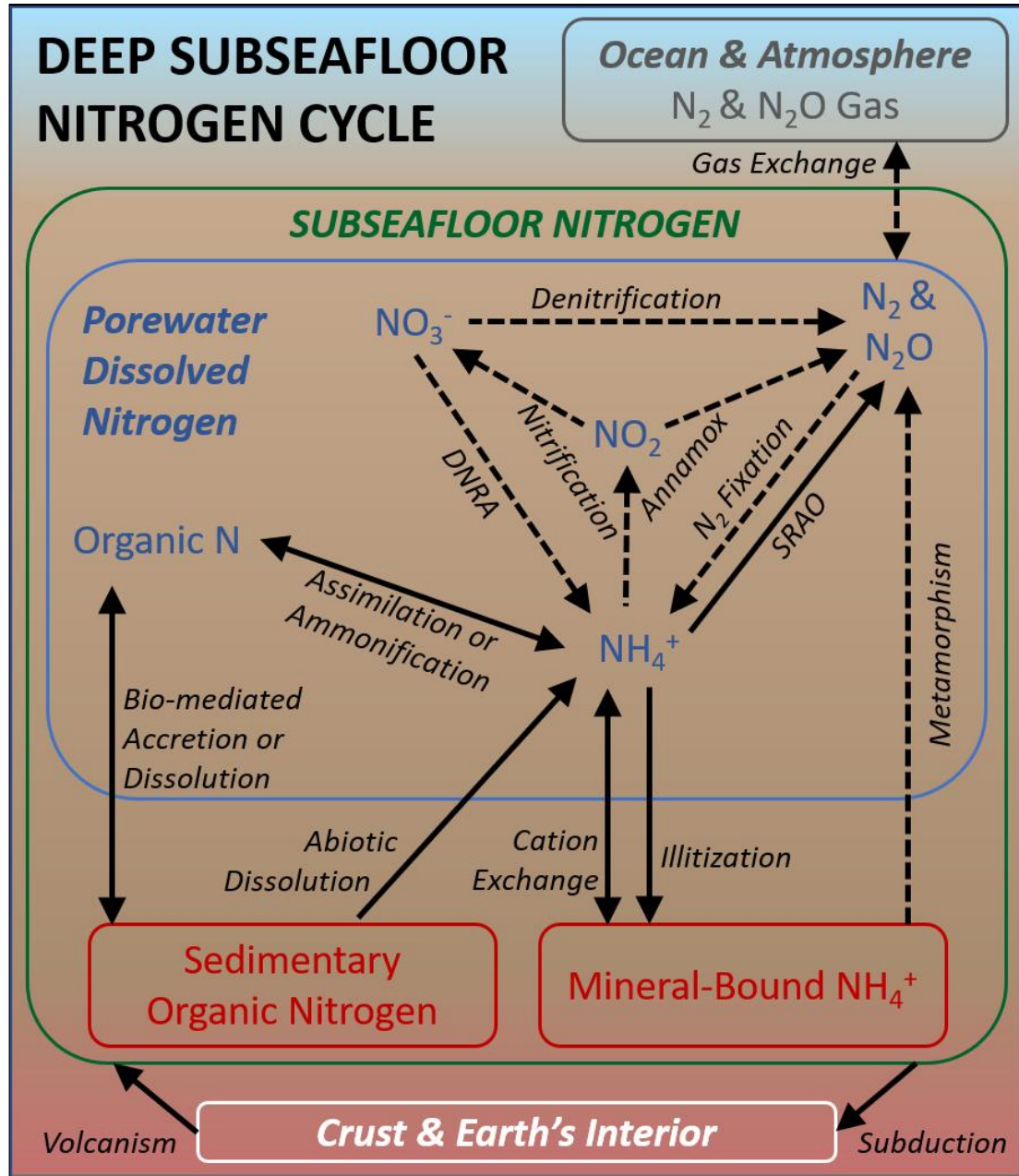
Figure 3.1. Anoxic subseafloor nitrogen transformations likely (solid arrows) and potentially (dashed arrows) occurring under the lithological and temperature regimes of IODP Site C0023. Dissolved nitrogen reservoirs are shown in blue (DON, NH_4^+, NO_3^-, NO_2^-, N_2, N_2O), solid reservoirs are shown in red (TON, NH_4^+), and nitrogen gas is shown in gray (N_2, N_2O). SRAO is Sulfate Reducing Ammonium Oxidation, Annamox is anaerobic ammonium oxidation, and DNRA is Dissimilatory Nitrate Reduction to Ammonium. Details of likely pathways can be found in *Table 3.1*.
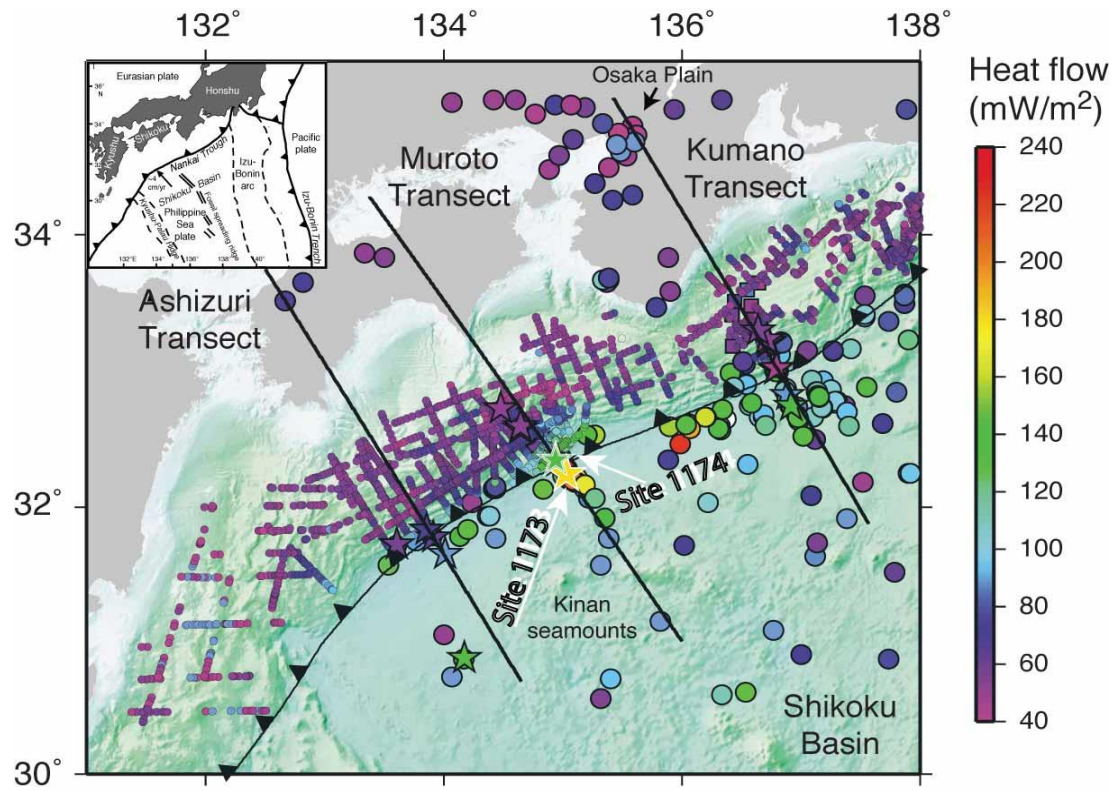
Figure 3.2. Site C0023 map and heat flow regime (Harris et al. 2013).
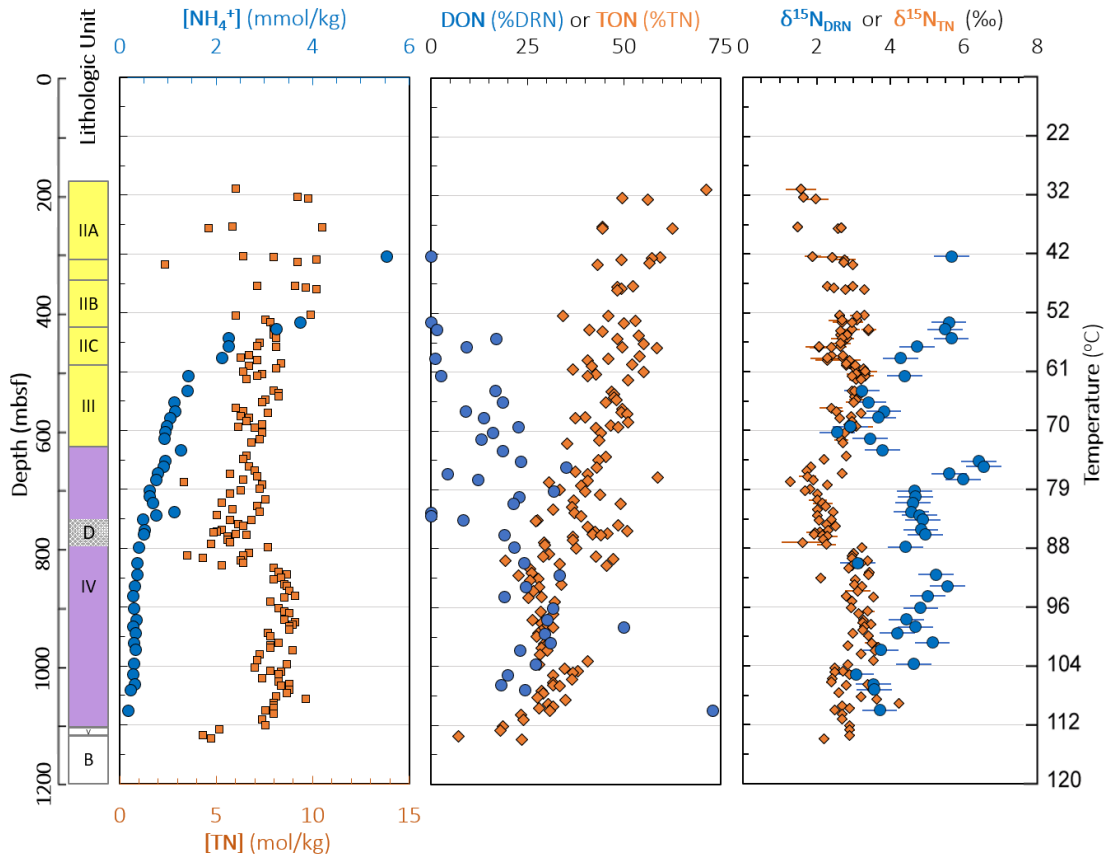
Figure 3.3. Site C0023 nitrogen measured from porewater (blue circles) and sediment (orange diamonds) as a function of depth and modeled *in-situ* temperature. Lithological units are shown at left with Upper (yellow, Units IIA-III) and Lower (purple, Unit IV) Shikoku Basin sediments distinguished, where D is décollement and B is basement (Heuer et al. 2017). Concentrations of [NH₄⁺] and [TN] are shown in the left panel (Heuer et al. 2017). Fractional abundance of organic to total nitrogen is shown in the center panel. Isotopic compositions ($\delta^{15}N_{DRN}$, $\delta^{15}N_{TN}$) are shown in the right panel will error bars of two standard deviations included in respective colors.
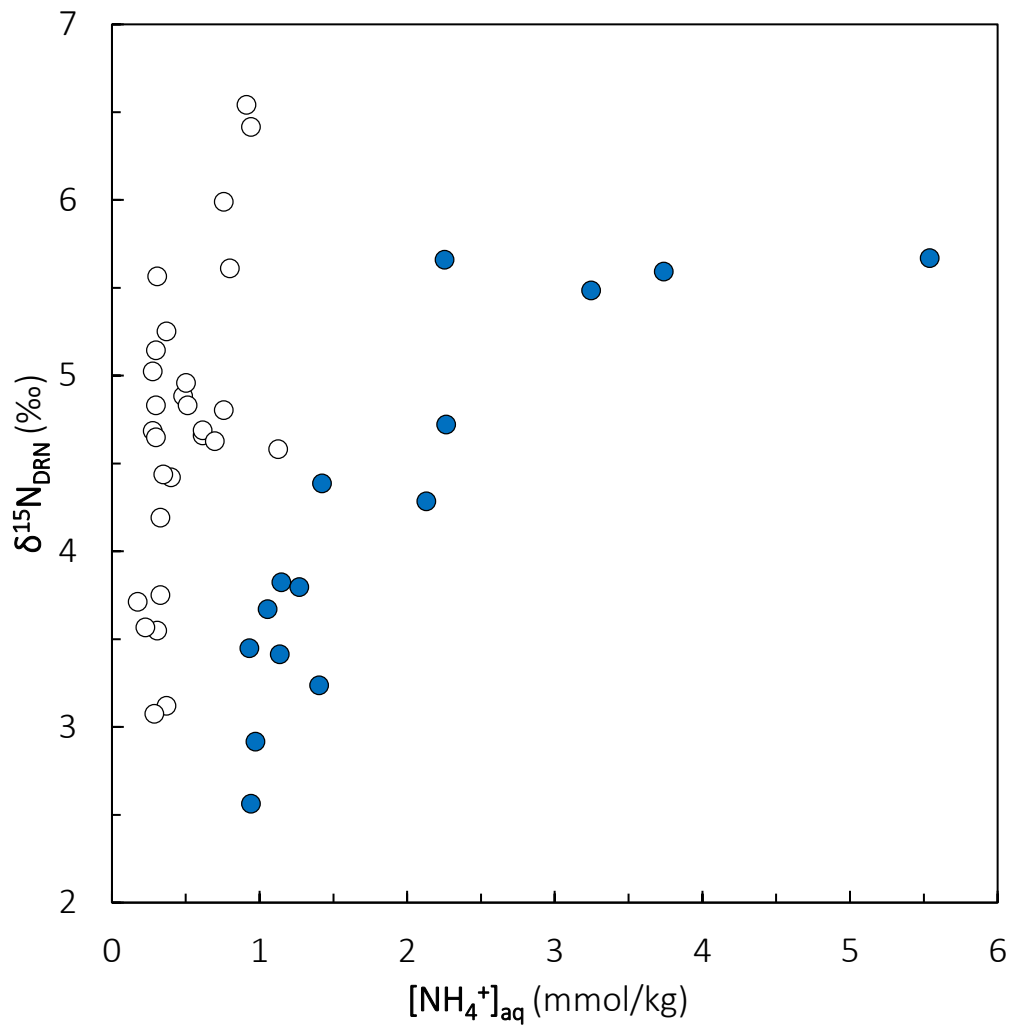
Figure 3.4. Nitrogen isotopes of DRN as a function of $[NH_4^+]_{aq}$. The Unit III/IV transition is distinguished with samples above 637 mbsf plotted in blue and those below in white.

1

Appendix 1.A: Porewater Data

Depth Below Seafloor

Sample depths below seafloor were adjusted from the measured distance below the core top by aligning geochemical, physical property, and dissolved oxygen measurements from KN223 long piston core (28.66m), gravity core (2.81m), and multicore data with bottom water data from the nearest WOCE site (A20 at 14.07N, 52.33W, 4932m water depth, temperature 1.5°C, salinity 34.84ppt, see *Table 1.2* for details).

Sulfate Analysis

Sulfate data collected on the KN223 cruise is reported as sulfate anomaly (☺), determined by ion chromatography. Reporting values as sulfate anomaly is more accurate as we ratio the peak areas determined by the IC directly to the chloride peak area, effectively circumventing much of the analytical error. The peak areas of seawater standard IAPSO, run in series with the samples, is used to calculate sulfate anomaly directly.

Conversion from sulfate anomaly (☺) to $[SO_4^{-2}]$:

$$☺ = \left(\frac{\left(\frac{[SO_4^{-2}]}{[Cl^-]} \right)_{sample}}{\left(\frac{[SO_4^{-2}]}{[Cl^-]} \right)_{IAPSO}} - 1 \right) 100$$

$$[SO_4^{-2}]_{sample} = \left([Cl^-]_{sample} \right) \left(\frac{☺}{100} + 1 \right) \left(\frac{[SO_4^{-2}]}{[Cl^-]} \right)_{IAPSO}$$

It is important to note that difficulties in pipetting during this cruise resulted in noisy IC chloride data so the chloride peak areas were used only to determine sulfate anomaly and were never converted to concentration.

To convert from sulfate anomaly to sulfate concentration where desired an independent chloride concentration is required. For KN223 long core samples, chloride concentrations were determined by titration. However, for the multicore & gravity core samples, no independent chloride concentrations were measured. Where titration-determined chloride concentrations were unavailable, sulfate concentration was determined using [Cl$^-$] of bottom water (from the closest WOCE stations) or the averages of the closest titrated chloride samples. Please see Table A1 for a breakdown of the chloride data used, and keep in mind that sulfate concentration data reported from a core without titrated chloride data has additional uncertainty.

Table A1. *Chloride concentration data source*

Core	Site 3	Site 10
Long	Titration	Titration
Gravity	LC Avg	N/A
Multicore	LC Avg	N/A

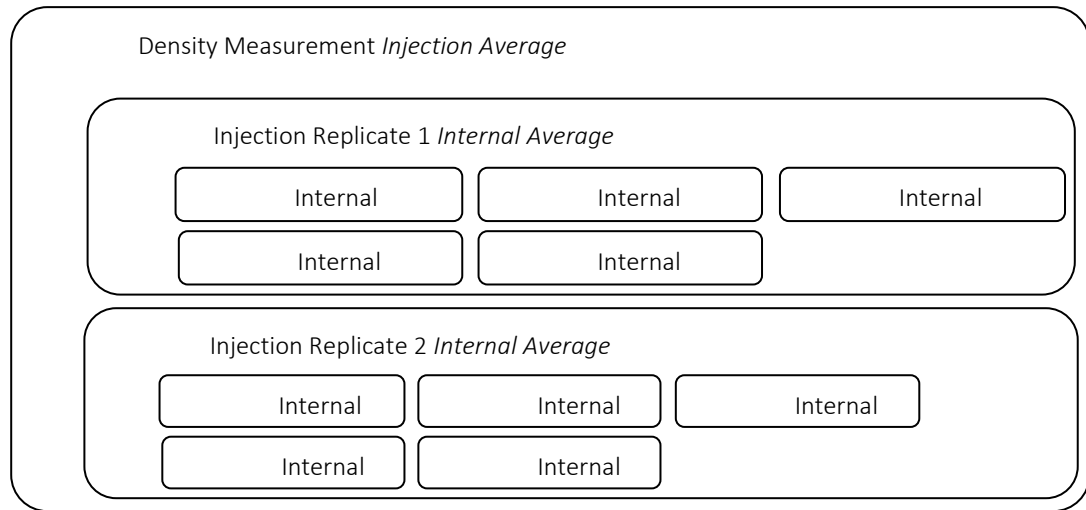**Titration:** aliquot of same sample run on the IC for sulfate anomaly was titrated for chloride
Some chloride samples were titrated post-expedition, notated with (PC)
LC Avg: shallowest titrated values from the long core were averaged to determine ~[Cl$^-$]
N/A: no core collected

Density Measurement Terminology

Figure A1. *Measurements within a final value, repeated for each component of the sequence.*

Appendix 1.B: Chloride from Porewater Density

Derivation

Starting with the definition of measured density ρ_{meas},

$$\rho_{meas} = \frac{m}{v} \tag{1}$$

where m is mass and v is volume, we separate mass and volume into two

contributions: prior to diagenesis (m^o, v^o) and post-diagenesis (m_i, v_i) where i refers to

a diagenetically varying chemical species.

$$\rho_{meas} = \frac{m^o + \Sigma_i \Delta m_i}{v^o + \Sigma_i \Delta v_i} \tag{2}$$

The mass and volume change associated with each solute i is given by

$$\Delta m_i = (n_i - n_i^o) Ar_i \tag{3a}$$

$$\Delta v_i = (n_i - n_i^o) V_i \tag{3b}$$

where n_i is the number of moles of solute i, Ar_i is the atomic (or molecular) weight,

and V_i is the partial molar volume of solute.

We assume chloride is conservative,

$$n_{Cl^-} = n_{Cl^-}^o \tag{4}$$

so that the post diagenesis and pre-diagenesis ratios, R_i and R_i^o, of a non-conservative

solute to chloride are

$$R_i = \frac{n_i}{n_{Cl^-}^o} \qquad R_i^o = \frac{n_i^o}{n_{Cl^-}^o} \tag{5}$$

with the change in the ratio due to diagenesis ΔR_i given by equation A6.

$$\Delta R_i = R_i - R_i^o = \frac{n_i}{n_{Cl^-}^o} - \frac{n_i^o}{n_{Cl^-}^o} = \frac{n_i - n_i^o}{n_{Cl^-}^o} \tag{6}$$

We solve equation 6 for the difference in the number of moles for a non-conservative solute.

$$n_i - n_i^o = n_{Cl^-}^o \Delta R_i \tag{7}$$

Substituting (7) into 3a,b

$$\Delta m_i = n_{Cl^-}^o \Delta R_i A r_i \tag{8a}$$

$$\Delta v_i = n_{Cl^-}^o \Delta R_i V_i \tag{8b}$$

And then substituting 8a,b into (2).

$$\rho_{meas} = \frac{m^o + n_{Cl^-}^o \sum_i \Delta R_i A r_i}{v^o + n_{Cl^-}^o \sum_i \Delta R_i V_i} \tag{9}$$

We divide the numerator and denominator of the right-hand-side of (9) by pre-diagenesis volume v^o.

$$\rho_{meas} = \frac{\rho^o + \frac{n_{Cl^-}^o}{v^o} \sum_i \Delta R_i A r_i}{1 + \frac{n_{Cl^-}^o}{v^o} \sum_i \Delta R_i V_i} \tag{10}$$

We substitute equation 11 into equation 10 to determine equation 12.

$$[Cl^-]^o = \frac{n_{Cl^-}^o}{v^o} \tag{11}$$

$$\rho_{meas} = \frac{\rho^o + [Cl^-]^o \sum_i \Delta R_i A r_i}{1 + [Cl^-]^o \sum_i \Delta R_i V_i} \tag{12}$$

Equation 12 can be solved for [Cl⁻]° since ρ_o is related to [Cl⁻]° by the equation of state for standard seawater. Over a small range in density and [Cl⁻]°, at constant temperature and pressure, the relationship is linear,

$$\rho^o = a[Cl^-]^o + \rho_{H_2O} \tag{13}$$

and can be substituted into (12) to give

$$\rho_{meas} = \frac{a[Cl^-]^o + \rho_{H_2O} + [Cl^-]^o \sum_i \Delta R_i A r_i}{1 + [Cl^-]^o \sum_i \Delta R_i V_i} \tag{14}$$

which, on rearrangement, gives equation 14.,

$$[Cl^-]^o = \frac{\rho_{meas} - \rho_{H_2O}}{a + \sum_i \Delta R_i Ar_i - \rho_{meas} \sum_i \Delta R_i V_i} \tag{14}$$

Effect of degassing samples on density

Note: when $Ar = \rho V$, no solute-dependent density change occurs.

Specific Cases (degassing during sample analysis):

Solute	Ar	ρV	$\Delta R^{BW}(Ar-\rho\varphi)$
Oxygen	1.59 E-02	3.18 E-02	-4.51 E-04
Nitrogen	1.40 E-02	3.38 E-02	-7.82 E-03
Argon	3.99 E-02	3.28 E-02	8.07 E-03

Effect of Diagenesis on Chloride Concentration

Since diagenesis changes the volume of the system due to the partial molar volumes of non-conservative solutes, the post-diagenesis chloride concentration [Cl⁻] will be different than the pre-diagenesis chloride, [Cl⁻]⁰. The change in [Cl⁻], Δ[Cl⁻], is given below.

$$\Delta[Cl^-] = [Cl^-] - [Cl^-]^o \tag{15}$$

$$\Delta[Cl^-] = n^o{}_{Cl^-} \left(\frac{1}{v} - \frac{1}{v^o}\right) \tag{16}$$

$$\Delta[Cl^-] = n^o \left(\frac{1}{(v^o + n^o{}_{Cl^-} \sum_i R_i V_i)} - \frac{1}{v^o}\right) \tag{17}$$

$$\Delta[Cl^-] = [Cl^-]^o \left(\frac{1}{(1 + [Cl^-]^o \sum_i R_i V_i)} - 1\right) \tag{18}$$

$$\Delta[Cl^-] = [Cl^-]^o \left(\frac{-[Cl^-]^o \sum_i R_i V_i}{(1 + [Cl^-]^o \sum_i R_i V_i)}\right) \tag{19}$$

$$\frac{\Delta[Cl^-]}{[Cl^-]^o} = \left(\frac{-[Cl^-]^o \sum_i R_i V_i}{(1 + [Cl^-]^o \sum_i R_i V_i)}\right) \tag{20}$$

$$[Cl^-] = \frac{\rho_{meas} - \rho_{H_2O}}{a + \sum_i \Delta R_i Ar_i - \rho_{H_2O} \sum_i \Delta R_i V_i} \qquad (21)$$

Iterating Initial Chloride

ΔR_i depends on chloride concentration. To avoid introducing uncertainty from low precision titration determined chloride concentrations, chloride concentrations used to calculate ΔR_i for density determined chloride are calculated as follows. Chloride concentration from density, *[Cl⁻](z,t,k),* is calculated as shown in equation 22 in terms of depth *z*, time *t*, and iteration *k*, where time equal to zero is modern porewater.

$$[Cl^-](z,0,k) = \frac{\rho_{meas} - \rho_{H_2O}}{a + \sum_i (\Delta R_i)^{k-1} Ar_i - \rho_{H_2O} \sum_i (\Delta R_i)^{k-1} V_i} \qquad (22)$$

On each iteration $\Delta R_i(z,k)$ is calculated using *[Cl⁻]°(z,0,k)* while *[Cl⁻]°(z,0,1)* for the first iteration is calculated using equation 13, which relates measured porewater density to chloride concentration using the equation of state for seawater assuming no diagenesis. On subsequent iterations (*k* > 1), *[Cl⁻]°(z,0,k)* is set to density determined chloride (eq 22) from the previous iteration, *[Cl⁻](z,0,k-1)*. Iteration continues until the difference between density determined chloride between one iteration and the next is indistinguishable within the uncertainty of *[Cl⁻](z,0,k)*.

Solute Ratio and Error Terms

   Sulfate

$$R_{SO_4^{-2},meas} = rloess\left(R_{SO_4^{-2}}\right), measured\ by\ ion\ chromatography$$

$$\varepsilon^2_{R_{SO_4^{-2}}} = \sigma^2_{R_{SO_4^{-2}}}$$

   Bicarbonate

$$R_{HCO_3^-,meas} = rloess\left(\frac{[HCO_3^-]}{rloess([Cl^-])}\right),$$

$$\frac{CO_2\ system\ solved\ from\ meas\ alkalinty\ and\ DIC}{measured\ by\ shipboard\ titration}$$

$$\varepsilon^2_{R_{HCO_3^-}} = \left(\frac{\sigma_{HCO_3^-}}{R_{HCO_3^-}}\right)^2 + \left(\frac{\sigma_{rloess[Cl^-]}}{rloess([Cl^-])}\right)^2$$

   Cations

$$R_{i,meas} = rloess\left(\frac{[i]}{rloess[Cl^-]}\right),\qquad \frac{measured\ by\ ion\ chromatography}{measured\ by\ shipboard\ titration}$$

$$\varepsilon^2_{[i]} = \left(\frac{\sigma_{R_{[i]}}}{R_{[i]}}\right)^2 + \left(\frac{\sigma_{rloess[Cl^-]}}{rloess([Cl^-])}\right)^2$$
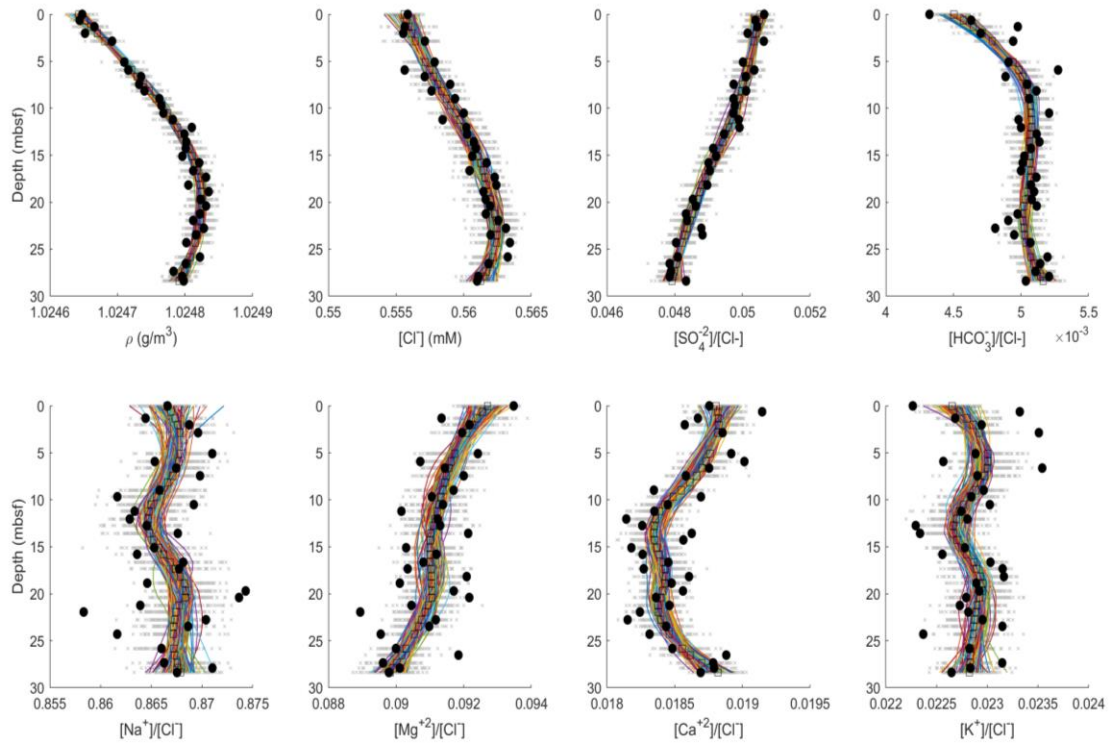
Figure A2. Measured and Monte Carlo porewater profiles from KN223 Site 03. Measured data is shown as solid circles, smoothed (and interpolated where necessary) rLoess fit to the measured data is shown as solid squares. Gray x's show Monte Carlo simulation normally distributed, randomly generated individual values at each depth, while colored lines show each Monte Carlo iteration's rLoess "smoothed" profile. The average and standard deviation of the colored lines interpolated at each measurement depth are used to evaluate the measurement error.

Appendix 1.C: Physical Properties
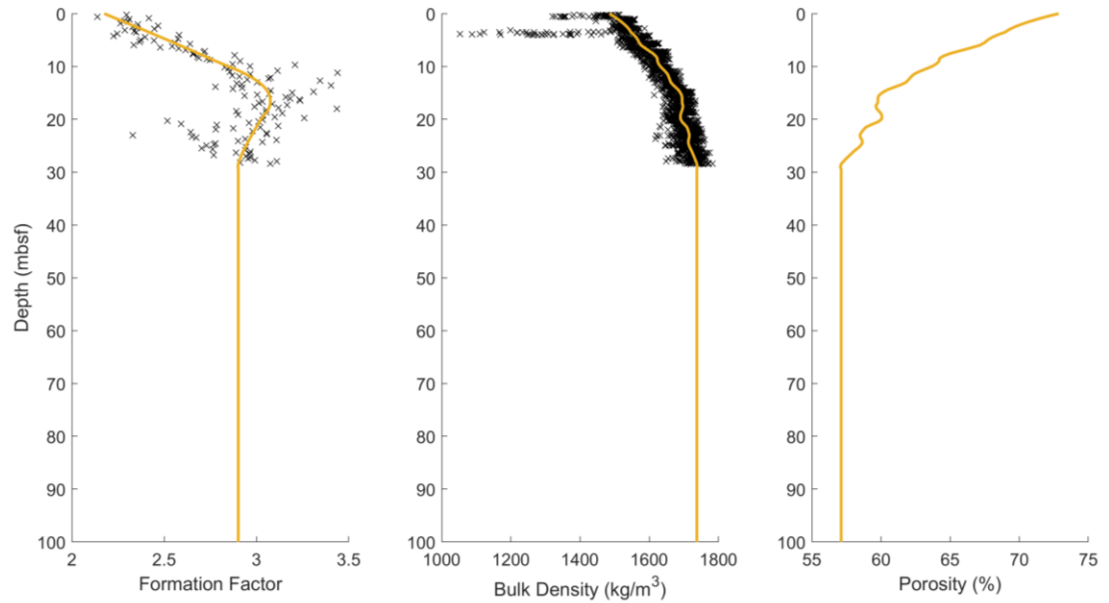
Figure A3. KN223 Site 03 physical properties for through modeled sediment, where measured data (black x's) is shown with its rloess fit (yellow line) for formation factor (left panel) measured by electric resistivity and bulk density (center panel) measured by gamma ray attenuation. Porosity calculated from measured and literature values in shown in the right panel.

Appendix 2.A: Oxidation of Dissolved Reduced Nitrogen

[NO_3^-] in each oxidized vial is determined by injecting 100 µL of sample or standard or 200 µL of blank into the reaction chamber. The linear fit of blanks and standards plotted with their known concentrations (0 µM for blanks; 20, 40, 60, and 100 µM for samples) of N against the peak area of their measured chemiluminescence chromatograms is used to confirm complete oxidation by POR and to convert peak areas of samples to NO_3^- concentrations.
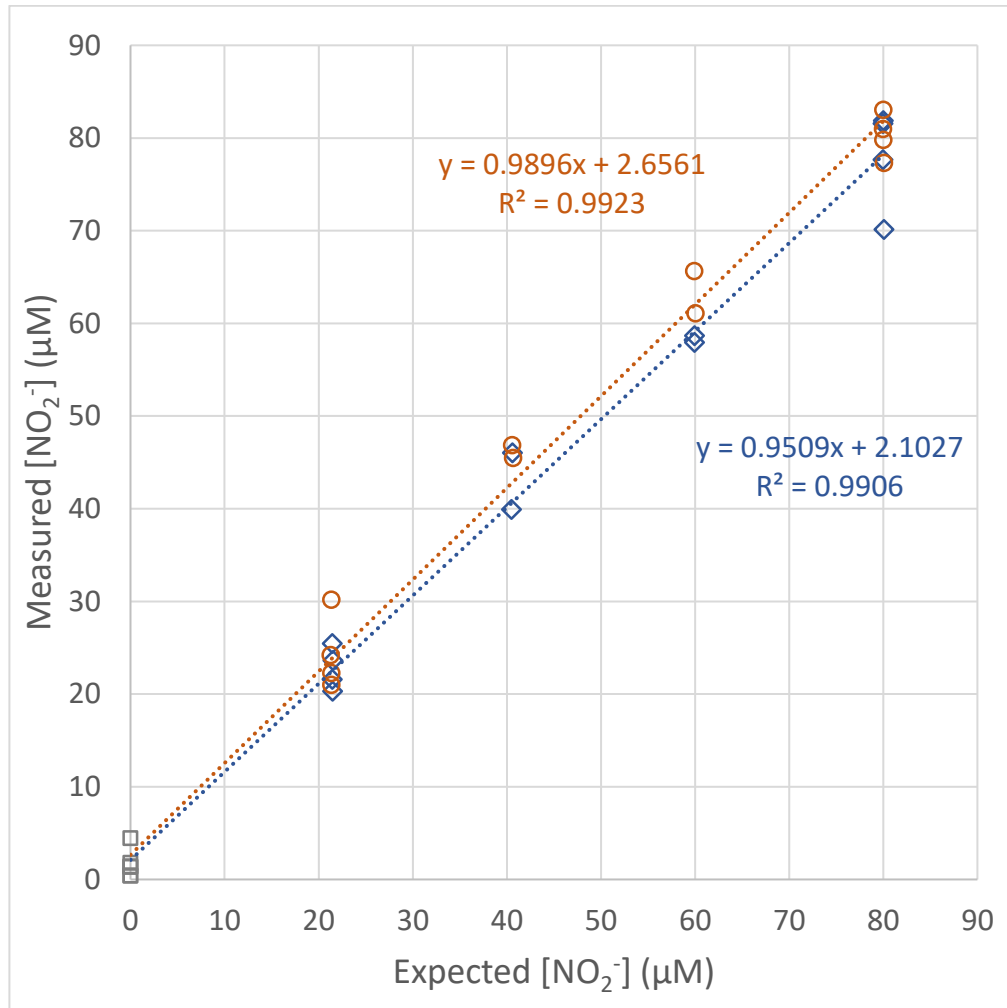
Figure A4. Expected and NO_x-box measured [NO_2] of IAEA N2 (orange circles) and ACA (blue diamonds) standards and procedural blanks (gray squares) from two weeks of POR batches. Linear fits to IAEA N2 (orange) and ACA (blue) are included with their equations and R^2 values.

REFERENCES

Adkins, J. F. and D. P. Schrag. 2001. "Pore Fluid Constraints on Deep Ocean Temperature and Salinity during the Last Glacial Maximum." *Geophysical Research Letters* 28(5):771–74.

Adkins, Jess F., Andrew P. Ingersoll, and Claudia Pasquero. 2005. "Rapid Climate Change and Conditional Instability of the Glacial Deep Ocean from the Thermobaric Effect and Geothermal Heating." *Quaternary Science Reviews* 24:581–94.

Adkins, Jess F., Katherine McIntyre, and Daniel P. Schrag. 2002. "The Salinity, Temperature, and Δ18O of the Glacial Deep Ocean." *Science* 298(5599):1769–73.

Adkins, Jess F. and Daniel P. Schrag. 2003. "Reconstructing Last Glacial Maximum Bottom Water Salinities from Deep-Sea Sediment Pore Fluid Profiles." *Earth and Planetary Science Letters* 216:109–23.

Andrews, Daniel and Barry T. Hargrave. 1984. "Close Interval Sampling of Interstitial Silicate and Porosity in Marine Sediments." *Geochimica et Cosmochimica Acta* 48:711–22.

Arndt, Sandra, B. B. Jørgensen, D. E. LaRowe, J. J. Middelburg, R. D. Pancost, and P. Regnier. 2013. "Quantifying the Degradation of Organic Matter in Marine Sediments: A Review and Synthesis." *Earth-Science Reviews* 123:53–86.

Berlekamp, Code-domain. 1997. "Pooled Standard Deviation." *IUPAC Compedium of Chemical Terminology* (2nd Edition):18–20.

Bernard, B. B., J. M. Brooks, and W. M. Sackett. 1976. "Natural Gas Seepage in the Gulf of Mexico." *Earth and Planetary Science Letters* 31(1):48–54.

Berner, Robert A. 2006. "Geological Nitrogen Cycle and Atmospheric N2 over Phanerozoic Time." *Geology*.

Boudreau, B. P. 1997. *Diagenetic Models and Their Implementation.* Berlin: Springer.

Bouttes, N., D. M. Roche, and D. Paillard. 2009. "Impact of Strong Deep Ocean Stratification on the Glacial Carbon Cycle." *Paleoceanography* 24(3):1–11.

Boyle, E. A. 2002. "Oceanography: Oceanic Salt Switch." *Science* 298(5599):1724–25.

Boyle, E. A. and L. D. Keigwin. 1982. "Deep Circulation of the North Atlantic over the Last 200,000 Years: Geochemical Evidence." *Science* 218(4574).

Boyle, E. A. and L. D. Keigwin. 1985. "Comparison of Atlantic and Pacific Paleochemical Records for the Last 215,000 Years: Changes in Deep Ocean Circulation and Chemical Inventories." *Earth and Planetary Science Letters* 76(1–2):135–50.

Braman, Robert S. and Steven A. Hendrix. 1989. "Nanogram Nitrite and Nitrate Determination in Environmental and Biological Materials by Vanadium(III) Reduction with Chemiluminescence Detection." *Analytical Chemistry* (61):2715–18.

Brandes, Jay A. and Allan H. Devol. 1997. "Isotopic Fractionation of Oxygen and Nitrogen in Coastal Marine Sediments." *Geochimica et Cosmochimica Acta*.

Broecker, Wallace, Elizabeth Clark, and Stephen Barker. 2008. "Near Constancy of the Pacific Ocean Surface to Mid-Depth Radiocarbon-Age Difference over the Last 20 Kyr." *Earth and Planetary Science Letters* 274:322–26.

Broecker, Wallace, Taro Takahashi, and Timothy Takahashi. 1985. "Sources and Flow Patterns of Deep-ocean Waters as Deduced from Potential Temperature, Salinity, and Initial Phosphate Concentration." *Journal of Geophysical Research* 90:6925–39.

Brovkin, Victor, Andrey Ganopolski, David Archer, and Stefan Rahmstorf. 2007. "Lowering of Glacial Atmospheric CO 2 in Response to Changes in Oceanic Circulation and Marine Biogeochemistry." *Paleoceanography and Paleoclimatology* 22(4):1–14.

Buchwald, C., K. Homola, A. J. Spivack, E. R. Estes, R. W. Murray, and S. D. Wankel. 2018. "Isotopic Constraints on Nitrogen Transformation Rates in the Deep Sedimentary Marine Biosphere." *Global Biogeochemical Cycles* 32(11):1688–1702.

Burke, Andrea, Andrew L. Stewart, Jess F. Adkins, Raffaele Ferrari, Malte F. Jansen, and Andrew F. Thompson. 2015. "The Glacial Mid-Depth Radiocarbon Bulge and Its Implications for the Overturning Circulation." *Paleoceanography* 1021–39.

Busigny, Vincent, Pierre Cartigny, and Pascal Philippot. 2011. "Nitrogen Isotopes in Ophiolitic Metagabbros: A Re-Evaluation of Modern Nitrogen Fluxes in Subduction Zones and Implication for the Early Earth Atmosphere." *Geochimica et Cosmochimica Acta* 75(23):7502–21.

Casciotti, Karen L. 2016. "Nitrogen and Oxygen Isotopic Studies of the Marine Nitrogen Cycle." *Annual Review of Marine Science* 8(1):379–407.

Charlesworth, John M. 1986. "Interaction of Clay Minerals with Organic Nitrogen Compounds Released by Kerogen Pyrolysis." *Geochimica et Cosmochimica Acta*.

Clark, Peter U., A. S. Dyke, J. D. Shakun, A. E. Carlson, J. Clark, B. Wohlfarth, J. X. Mitrovica, S. W. Hostetler, and A. M. McCabe. 2009. "The Last Glacial Maximum." *Science* 325(5941):710–14.

Clark, Peter U. and Alan C. Mix. 2002. "Ice Sheets and Sea Level of the Last Glacial Maximum." *Quaternary Science Reviews* 21:1–7.

Clark, Peter U., Jeremy D. Shakun, Paul A. Baker, Patrick J. Bartlein, Simon Brewer, Ed Brook, Anders E. Carlson, Hai Cheng, Darrell S. Kaufman, Zhengyu Liu, Thomas M. Marchitto, Alan C. Mix, Carrie Morrill, Bette L. Otto-Bliesner, Katharina Pahnke, James M. Russell, Cathy Whitlock, Jess F. Adkins, Jessica L. Blois, Jorie Clark, Steven M. Colman, William B. Curry, Ben P. Flower, Feng He, Thomas C. Johnson, Jean Lynch-Stieglitz, Vera Markgraf, Jerry McManus, Jerry X. Mitrovica, Patricio I. Moreno, and John W. Williams. 2012. "Global Climate Evolution during the Last Deglaciation." *Proceedings of the National Academy of Sciences of the United States of America* 109(19):17–19.

Cleveland, William S. and Susan J. Devlin. 1988. "Locally Weighted Regression: An Approach to Regression Analysis by Local Fitting AU - Cleveland, William S." *Journal of the American Statistical Association* 83(403):596–610.

Curry, William, James Broda, Lloyd Keigwin, Gregory Mountain, and Nicklas Pisias. 2008. "A New Long Coring System for R/V Knorr." *Eos* 89(15):142–43.

Curry, William and D. W. Oppo. 2005. "Glacial Water Mass Geometry and the Distribution of D 13 C of 2 CO 2 in the Western Atlantic Ocean."

Paleoceanography 20:1–13.

Cutler, K. B., R. L. Edwards, F. W. Taylor, H. Cheng, J. Adkins, C. D. Gallup, P. M. Cutler, G. S. Burr, and A. L. Bloom. 2003. "Rapid Sea-Level Fall and Deep-Ocean Temperature Change since the Last Interglacial Period." 206.

D'Hondt, Steven, Robert Pockalny, Victoria M. Fulfer, and Arthur J. Spivack. 2019. "Subseafloor Life and Its Biogeochemical Impacts." *Nature Communications* 10(1):1–13.

DeMaster, David J. 2002. "The Accumulation and Cycling of Biogenic Silica in the Southern Ocean: Revisiting the Marine Silica Budget." *Deep-Sea Research Part II: Topical Studies in Oceanography* 49(16):3155–67.

Divins, D. L. 2003. *Total Sediment Thickness of the World's Oceans and Marginal Seas*. Boulder, CO.

Edmond, John M. 1970. "High Precision Determination of Titration Alkalinity and Total Carbon Dioxide Content of Sea Water by Potentiometric Titration." *Deep-Sea Research and Oceanographic Abstracts* 17(4):737–50.

Edmond, John M. and J. M. T. M. Gieskes. 1970. "On the Calculation of the Degree of Saturation of Sea Water with Respect to Calcium Carbonate under in Situ Conditions." *Geochimica et Cosmochimica Acta* 34(12):1261–91.

Erbacher, J., D. C. Mosher, and M. J. Malone. 2004. "Leg 207." *Proceedings of the Ocean Drilling Program: International Reports*.

Feistel, R., S. Weinreben, H. Wolf, S. Seitz, P. Spitzer, B. Adel, G. Nausch, B. Schneider, and D. G. Wright. 2010. "Density and Absolute Salinity of the Baltic Sea 2006 – 2009." *Ocean Science* 6(1):3–24.

Ferrari, Raffaele, Malte F. Jansen, Jess F. Adkins, Andrea Burke, Andrew L. Stewart, and Andrew F. Thompson. 2014. "Antarctic Sea Ice Control on Ocean Circulation in Present and Glacial Climates." *Proceedings of the National Academy of Sciences* 111(24).

Galbraith, Eric and Casimir Lavergne. 2019. "Response of a Comprehensive Climate Model to a Broad Range of External Forcings: Relevance for Deep Ocean Ventilation and the Development of Late Cenozoic Ice Ages." *Climate Dynamics* 52(1–2):653–79.

Gehlen, M. and W. Van Raaphorst. 2002. "The Role of Adsorption-Desorption Surface Reactions in Controlling Interstitial Si(OH)4 Concentrations and Enhancing Si(OH)4 Turn-over in Shallow Shelf Seas." *Continental Shelf Research* 22(10):1529–47.

Govin, Aline, Elisabeth Michel, Laurent Labeyrie, Claire Waelbroeck, Fabien Dewilde, and Eystein Jansen. 2009. "Evidence for Northward Expansion of Antarctic Bottom Water Mass in the Southern Ocean during the Last Glacial Inception." *Paleoceanography* 24:1–14.

Graham, David W., Bruce H. Corliss, Michael L. Bender, and Lloyd Keigwin. 1981. "Carbon and Oxygen Isotopic Disequilibria of Recent Deep-Sea Benthic Foraminifera*." *Marine Micropaleontology* 6:483–97.

Haendel, Dietmar, Karl Mühle, Horst Michael Nitzsche, Gottfried Stiehl, and Ulrich Wand. 1986. "Isotopic Variations of the Fixed Nitrogen in Metamorphic Rocks."

Geochimica et Cosmochimica Acta 50(5):749–58.

Halama, Ralf, Gray E. Bebout, Timm John, and Marco Scambelluri. 2014. "Nitrogen Recycling in Subducted Mantle Rocks and Implications for the Global Nitrogen Cycle." *International Journal of Earth Sciences* 103(7):2081–99.

Harris, Rachel. 2020. "Tracing Piezophilic Anaerobic Methane Oxidation in Deep Sub-Seafloor Microbial Communities from IODP 370 Site C0023A in the Nankai Trough Accretionary Complex." Princeton.

Harris, Robert, Makoto Yamano, Masataka Kinoshita, Glenn Spinelli, Hideki Hamamoto, and Juichiro Ashi. 2013. "A Synthesis of Heat Flow Determinations and Thermal Modeling along the Nankai Trough, Japan." *Journal of Geophysical Research: Solid Earth* 118(6):2687–2702.

Heuer, V. B., F. Inagaki, Y. Morono, Y. Kubo, L. Maeda, A. Spivack, B. Viehweger, T. Treude, F. Beulig, F. Schubotz, S. Tonai, S. Bowden, M. Cramm, S. Henkel, T. Hirose, K. Homola, T. Hoshino, A. Ijiri, H. Imachi, N. Kamiya, M. Kaneko, L. Lagostina, H. M, and K. U. Hinrichs. 2020. "Temperature Limits to Deep Subseafloor Life in the Nankai Trough Subduction Zone." *Science* in press.

Heuer, V. B., Fumio Inagaki, Yuki Morono, Yusuke Kubo, L. Maeda, and Expedition 370 Scientists. 2017. "Temperature Limit of the Deep Biosphere off Muroto." *Proceedings of the International Ocean Discovery Program* 370(November).

Hinrichs, K. U., F. Inagaki, V. B. Heuer, M. Kinoshita, Y. Morono, and Y. Kubo. 2016. "Expedition 370 Scientific Prospectus T-Limit of the Deep Biosphere off Muroto (T-Limit)." *International Ocean Discovery Program*.

Hoch, Matthew P., Marilyn L. Fogel, and David L. Kirchman. 1992. "Isotope Fractionation Associated with Ammonium Uptake by a Marine Bacterium." *Limnology and Oceanography*.

Hoch, Matthew P., Richard A. Snyder, Luis A. Cifuentes, and Richard B. Coffin. 1996. "Stable Isotope Dynamics of Nitrogen Recycled during Interactions among Marine Bacteria and Protists." *Marine Ecology Progress Series*.

Holloway, JoAnn M. and Randy A. Dahlgren. 2002. "Nitrogen in Rock: Occurrences and Biogeochemical Implications." *Global Biogeochemical Cycles*.

Holloway, Max D., Louise C. Sime, Joy S. Singarayer, Julia C. Tindall, and Paul J. Valdes. 2016. "Reconstructing Paleosalinity from Δ18O: Coupled Model Simulations of the Last Glacial Maximum, Last Interglacial and Late Holocene." *Quaternary Science Reviews* 131:350–64.

Holm, Nils G. and Anna Neubeck. 2009. "Reduction of Nitrogen Compounds in Oceanic Basement and Its Implications for HCN Formation and Abiotic Organic Synthesis." *Geochemical Transactions*.

Homola, K., A. J. Spivack, S. D'Hondt, E. Estes, T. Insua, C. McKinley, R. Murray, R. Pockalny, R. Robinson, and J. Sauvage. 2015. "Preformed Nitrate In The Glacial North Atlantic." Pp. PP43A-2254 in *AGU Fall Meeting*.

Inagaki, Fumio, Masa Kinoshita, Akira Ijiri, Keita Akiyama, Verena B. Heuer, Kira Homola, Carmen Li, Takashi Morisawa, Yuki Morono, Donald Pan, Tianhaozhe Sun, Man-Yin Tsang, Toki Tomohiro, and IODP Expedition 370 Scientists. 2019. "KAIREI KR18-04 Cruise Report: Recovery of 1.5 Years-Temperature Observatory

Data and Shallow Piston-Core Sediments from IODP Site C0023." *JAMSTEC*.

Insua, T. L., A. J. Spivack, D. Graham, S. D'Hondt, and K. Moran. 2014. "Reconstruction of Pacific Ocean Bottom Water Salinity during the Last Glacial Maximum." *Geophysical Research Letters* 41(8):2914–20.

Ito, Takamitsu and Michael J. Follows. 2013. "Air-Sea Disequilibrium of Carbon Dioxide Enhances the Biological Carbon Sequestration in the Southern Ocean." *Global Biogeochemical Cycles*.

Jansen, Malte F. 2017. "Glacial Ocean Circulation and Stratification Explained by Reduced Atmospheric Temperature." *Proceedings of the National Academy of Sciences of the United States of America* 114(1):45–50.

Jansen, Malte F. and Louis Philippe Nadeau. 2016. "The Effect of Southern Ocean Surface Buoyancy Loss on the Deep-Ocean Circulation and Stratification." *Journal of Physical Oceanography* 46(11):3455–70.

Jørgensen, Bo Barker and Ian P. G. Marshall. 2016. "Slow Microbial Life in the Seabed."

Kallmeyer, Jens, Robert Pockalny, Rishi Ram, David C. Smith, and Steven D. Hondt. 2012. "Global Distribution of Microbial Abundance and Biomass in Subseafloor Sediment." 109(40):1–4.

Keigwin, Lloyd D. 2004. "Radiocarbon and Stable Isotope Constraints on Last Glacial Maximum and Younger Dryas Ventilation in the Western North Atlantic." *Paleoceanography* 19(4):1–15.

Keigwin, Lloyd D. and Stephen A. Swift. 2017. "Carbon Isotope Evidence for a Northern Source of Deep Water in the Glacial Western North Atlantic." 114(11):2831–35.

Kim, Jinwook, Hailiang Dong, Kiho Yang, Hanbeom Park, W. Crawford Elliott, Arthur Spivack, Tae-hee Koo, Gilyoung Kim, Yuki Morono, Susann Henkel, Fumio Inagaki, Qiang Zeng, Tatsuhiko Hoshino, and Verena B. Heuer. 2019. "Naturally Occurring, Microbially Induced Smectite-to-Illite Reaction." *Geology* 47(6):1–5.

Knapp, Angela N., Daniel M. Sigman, and Fredric Lipschultz. 2005. "N Isotopic Composition of Dissolved Organic Nitrogen and Nitrate at the Bermuda Atlantic Time-Series Study Site." *Global Biogeochemical Cycles* 19(1):1–15.

Kobayashi, Hidetaka, Ayako Abe-Ouchi, and Akira Oka. 2015. "Role of Southern Ocean Stratification in Glacial Atmospheric CO2 Reduction Evaluated by a Three-Dimensional Ocean General Circulation Model." *Paleoceanography* 30(9):1202–16.

Koltermann, Klaus P., Viktor Gouretski, and Kai Jancke. 2011. *Hydrographic Atlas of the World Ocean Circulation Experiment (WOCE) Volume 3: Atlantic Ocean*. Vol. 3.

Koo, Tae hee, Young nam Jang, Toshihiro Kogure, Jae Hoon Kim, Byung Cheol Park, Don Sunwoo, and Jin wook Kim. 2014. "Structural and Chemical Modification of Nontronite Associated with Microbial Fe(III) Reduction: Indicators of 'Illitization.'" *Chemical Geology* 377:87–95.

Kwon, Eun Young, Mathis P. Hain, Daniel M. Sigman, Eric D. Galbraith, Jorge L. Sarmiento, and J. R. Toggweiler. 2012. "North Atlantic Ventilation of Southern-Sourced Deep Water in the Glacial Ocean." *Paleoceanography* 27(2):1–12.

Labidi, J., P. H. Barry, D. V. Bekaert, M. W. Broadley, B. Marty, T. Giunta, O. Warr, B. Sherwood Lollar, T. P. Fischer, G. Avice, A. Caracausi, C. J. Ballentine, S. A.

Halldórsson, A. Stefánsson, M. D. Kurz, I. E. Kohl, and E. D. Young. 2020. "Hydrothermal 15N15N Abundances Constrain the Origins of Mantle Nitrogen." *Nature* 580(7803):367–71.

Lehmann, Moritz F., Stefano M. Bernasconi, Alberto Barbieri, and Judith A. McKenzie. 2002. "Preservation of Organic Matter and Alteration of Its Carbon and Nitrogen Isotope Composition during Simulated and in Situ Early Sedimentary Diagenesis." *Geochimica et Cosmochimica Acta* 66(20):3573–84.

Lewis, E. L. and R. G. Perkin. 1978. "Salinity: Its Definition and Calculation." *Journal of Geophysical Research* 83(C1):466.

Li, Long, Gray E. Bebout, and Bruce D. Idleman. 2007. "Nitrogen Concentration and Δ15N of Altered Oceanic Crust Obtained on ODP Legs 129 and 185: Insights into Alteration-Related Nitrogen Enrichment and the Nitrogen Subduction Budget." *Geochimica et Cosmochimica Acta*.

Lund, D. C., J. F. Adkins, and R. Ferrari. 2011. "Abyssal Atlantic Circulation during the Last Glacial Maximum: Constraining the Ratio between Transport and Vertical Mixing." *Paleoceanography* 26(1):1–19.

Lynch-Stieglitz, Jean, Jess F. Adkins, William B. Curry, Trond Dokken, Ian R. Hall, Juan Carlos Herguera, Joël J. Hirschi, Elena V Ivanova, Catherine Kissel, Olivier Marchal, Thomas M. Marchitto, I. Nicholas Mccave, and Jerry F. Mcmanus. 2007. "Atlantic Meridional Overturning Circulation During the Last Glacial Maximum." *Science* 316.

Macko, Stephen A., Marilyn L. Fogel, P. E. Hare, and T. C. Hoering. 1987. "Isotopic Fractionation of Nitrogen and Carbon in the Synthesis of Amino Acids by Microorganisms." *Chemical Geology: Isotope Geoscience Section* 65(1):79–92.

Mallik, Ananya, Yuan Li, and Michael Wiedenbeck. 2018. "Nitrogen Evolution within the Earth's Atmosphere–Mantle System Assessed by Recycling in Subduction Zones." *Earth and Planetary Science Letters* 482:556–66.

Manheim. 1974. "Comparative Studies on Extraction of Sediment Interstitial Waters: Discussion and Comment on the Current State of Interstitial Water Studies." *Clays and Clay Minerals* 22(4):337–43.

Manheim, FT, LS Waterman, CC Woo, and FL Sayles. 1974. "35. INTERSTITIAL WATER STUDIES ON SMALL CORE SAMPLES, LEG 23 (RED SEA)." *Interstitial Water Studies*.

Matsumoto, Katsumi. 2017. "Tantalizing Evidence for the Glacial North Atlantic Bottom Water." *Proceedings of the National Academy of Sciences* 114(11):2794–96.

Mcdougall, T. J., R. Feistel, F. J. Millero, D. R. Jackett, D. G. Wright, B. a King, G. M. Marion, C-t a Chen, and P. Spitzer. 2009. "The International Thermodynamic Equation Of Seawater 2010 (TEOS-10): Calculation and Use of Thermodynamic Properties." *IOCCP, ICPO Publication Series No. 134* (Report No. 14).

McDuff, R. E., J. M. Gieskes, and J. R. Lawrence. 1978. "Interstitial Water Studies, Leg 42A." *Initial Reports Deep Sea Drilling Projects* 42:561–68.

McDuff, RE. 1985. "The Chemistry of Interstitial Waters, Deep-Sea Drilling Project Leg-86." *Initial Reports of the Deep Sea Drilling Project* 86:675–87.

Meunier, A., B. Lanson, and D. Beaufort. 2000. "Vermiculitization of Smectite

Interfaces and Illite Layer Growth as a Possible Dual Model for Illite-Smectite Illitization in Diagenetic Environments: A Synthesis." *Clay Minerals*.

Miller, M. D., J. F. Adkins, D. Menemenlis, and M. P. Schodlok. 2012. "The Role of Ocean Cooling in Setting Glacial Southern Source Bottom Water Salinity." 27(August):1–16.

Millero, Frank J., Rainer Feistel, Daniel G. Wright, and Trevor J. Mcdougall. 2008. "The Composition of Standard Seawater and the Definition of the Reference-Composition Salinity Scale." *Deep Sea Research Part I: Oceanographic Research Papers* 55(1):50–72.

Millero, Frank J. and Fen Huang. 2013. "Molal Volumes and Compressibilities of Salts in Seawater." *Geochimica et Cosmochimica Acta* 104:19–28.

Millero, Frank J., Fen Huang, Nancy Williams, Jason Waters, and Ryan Woosley. 2009. "The Effect of Composition on the Density of South Pacific Ocean Waters." *Marine Chemistry* 114(1–2):56–62.

Mix, Alan C., Edouard Bard, and Ralph Schneider. 2001. "Environmental Processes of the Ice Age : Land , Oceans , Glaciers (EPILOG)." *Quaternary Science Reviews* 20:627–57.

Moore, G. F., A. Taira, A. Klaus, and Et. Al. 2001. "Site 1174." *Proceedings of the Ocean Drilling Program, Inital Reports* 190.

Morono, Y., F. Inagaki, V. B. Heuer, Y. Kubo, L. Maeda, S. Bowden, M. Cramm, S. Henkel, T. Hirose, K. Homola, T. Hoshino, A. Ijiri, H. Imachi, N. Kamiya, M. Kaneko, L. Lagostina, H. Manners, H. L. McClelland, K. Metcalfe, N. Okutsu, D. Pan, M. J. Raudsepp, J. Sauvage, F. Schubotz, A. Spivack, S. Tonai, T. Treude, M. Y. Tsang, B. Viehweger, D. T. Wang, E. Whitaker, Y. Yamamoto, and K. Yang. 2017. "Expedition 370 Methods." *Proceedings of the International Ocean Discovery Program* 370(November).

Müller, R. Dietmar, Maria Sdrolias, Carmen Gaina, and Walter R. Roest. 2008. "Age, Spreading Rates, and Spreading Asymmetry of the World's Ocean Crust." *Geochemistry, Geophysics, Geosystems* 9(4):1–19.

Munk, Walter. 1950. "On the Wind-Driven Ocean Circulation." *Journal of Meteorology* 7(2).

Nadeau, Louis Philippe, Raffaele Ferrari, and Malte F. Jansen. 2019. "Antarctic Sea Ice Control on the Depth of North Atlantic Deep Water." *Journal of Climate* 32(9):2537–51.

Negre, César, Rainer Zahn, Alexander L. Thomas, Pere Masqué, Gideon M. Henderson, Gema Martínez-Méndez, Ian R. Hall, and José L. Mas. 2010. "Reversed Flow of Atlantic Deep Water during the Last Glacial Maximum." *Nature* 468(7320):84–88.

Parkes, R. John, Barry Cragg, Erwan Roussel, Gordon Webster, Andrew Weightman, and Henrik Sass. 2014. "A Review of Prokaryotic Populations and Processes in Sub-Seafloor Sediments, Including Biosphere: Geosphere Interactions." *Marine Geology* 352:409–25.

Peltier, W. R. and R. G. Fairbanks. 2006. "Global Glacial Ice Volume and Last Glacial Maximum Duration from an Extended Barbados Sea Level Record." *Quaternary Science Reviews* 25(23–24):3322–37.

Petit, J. R., J. Jouzel, D. Raynaud, N. I. Barkov, J. M. Barnola, I. Basile, M. Bender, J. Chappellaz, M. Davis, G. Delaygue, M. Delmotte, V. M. Kotiyakov, M. Legrand, V. Y. Lipenkov, C. Lorius, L. Pépin, C. Ritz, E. Saltzman, and M. Stievenard. 1999. "Climate and Atmospheric History of the Past 420,000 Years from the Vostok Ice Core, Antarctica." *Nature* 399(6735):429–36.

Pilson, Michael E. Q. 2015. *An Introduction to the Chemistry of the Sea*.

Prokopenko, M. G., D. E. Hammond, L. Stott, and A. J. Spivack. 2004. "Nitrogen Isotopic Composition of Ammonium Released during Diagenesis of Organic Matter under Steady-State and Non-Steady State Conditions in Marine Anoxic Sediments." *American Geophysical Union, Fall Meeting 2004, Abstract Id. PP51G-04*.

Prokopenko, Maria G., Douglas E. Hammond, and Lowell Stott. 2006. "Lack of Isotopic Fractionation of Δ15N of Organic Matter during Long-Term Diagenesis in Marine Sediments, ODP Leg 202, Sites 1234 and 1235." *Proceedings of the Ocean Drilling Program: Scientific Results* 202(October 2004).

Robinson, Allan and Henry Stommel. 1959. "The Oceanic Thermocline." *Tellus* 3.

Robinson, Rebecca S., Markus Kienast, Ana Luiza Albuquerque, Mark Altabet, Sergio Contreras, Ricardo De Pol Holz, Nathalie Dubois, Roger Francois, Eric Galbraith, Ting Chang Hsu, Tara Ivanochko, Samuel Jaccard, Shuh Ji Kao, Thorsten Kiefer, Stephanie Kienast, Moritz Lehmann, Philippe Martinez, Matthew McCarthy, Jürgen Möbius, Tom Pedersen, Tracy M. Quan, Evgeniya Ryabenko, Andreas Schmittner, Ralph Schneider, Aya Schneider-Mor, Masahito Shigemitsu, Dan Sinclair, Christopher Somes, Anja Studer, Robert Thunell, and Jin Yu Yang. 2012. "A Review of Nitrogen Isotopic Alteration in Marine Sediments." *Paleoceanography* 27(4).

Sadofsky, Seth J. and Gray E. Bebout. 2000. "Ammonium Partitioning and Nitrogen-Isotope Fractionation among Coexisting Micas during High-Temperature Fluid-Rock Interactions: Examples from the New England Appalachians." *Geochimica et Cosmochimica Acta* 64(16):2835–49.

Sarmiento, Jorge L. and Nicolas Gruber. 2002. "SINKS FOR ANTHROPOGENIC CARBON." *Physics Today* 30–36.

Schink, David R., Kent A. Fanning, and Michael E. Q. Pilson. 1974. "Dissolved Silica in the Upper Pore Waters of the Atlantic Ocean Floor." *Journal of Geophysical Research* 79(15):2243–50.

Schmidt, Frauke, Boris P. Koch, Marcus Elvert, Gunnar Schmidt, Matthias Witt, and Kai-uwe Hinrichs. 2011. "Diagenetic Transformation of Dissolved Organic Nitrogen Compounds under Contrasting Sedimentary Redox Conditions in the Black Sea." *Environmental Science and Technology* 45:5223–29.

Schmittner, Andreas and Eric D. Galbraith. 2008. "Glacial Greenhouse-Gas Fluctuations Controlled by Ocean Circulation Changes." *Nature* 456(7220):373–76.

Schrag, D. P., D. J. Depaolo, and F. M. Richter. 1992. "Oxygen Isotope Exchange in a 2-Layer Model of Oceanic-Crust." *Earth and Planetary Science Letters* 111(2–4):305–17.

Schroeder, Paul and A. A. McLain. 1998. "Illite-Smectites and the Influence of Burial

Diagenesis on the Geochemical Cycling of Nitrogen." *Clay Minerals* 33(4):539–46.

Schrum, Heather N., Arthur J. Spivack, Miriam Kastner, and Steven D. Hondt. 2009. "Sulfate-Reducing Ammonium Oxidation : A Thermodynamically Feasible Metabolic Pathway in Subseafl Oor Sediment." *Geology* 37(10):939–42.

Sepúlveda, Julio, Jens Wendler, Arne Leider, Hans Joachim Kuss, Roger E. Summons, and Kai Uwe Hinrichs. 2009. "Molecular Isotopic Evidence of Environmental and Ecological Changes across the Cenomanian-Turonian Boundary in the Levant Platform of Central Jordan." *Organic Geochemistry* 40(5):553–68.

Siddall, M., E. Rohling, W. Thompson, and C. Waelbroeck. 2008. "MIS 3 Sea Level Fluctuations: Data Synthesis and New Outlook." *Reviews of Geophysics* 46(2007):1–29.

Siegenthaler, Urs, Thomas F. Stocker, and Eric Monnin. 2005. "Stable Carbon Cycle – Climate Relationship During the Late Pleistocene." *Science* 310:1313–18.

Sigman, D. M., K. L. Casciotti, M. Andreani, C. Barford, M. Galanter, and J. K. Böhlke. 2001. "A Bacterial Method for the Nitrogen Isotopic Analysis of Nitrate in Seawater and Freshwater." *Analytical Chemistry* 73(17):4145–53.

Sigman, Daniel M. and Edward A. Boyle. 2000. "Glacial/Interglacial Variations in Atmospheric Carbon Dixoide." *Nature* 407(October):859–69.

Sigman, Daniel M., Mathis P. Hain, and Gerald H. Haug. 2010. "The Polar Ocean and Glacial Cycles in Atmospheric CO2 Concentration." *Nature* 466(7302):47–55.

Sijinkumar, A. V, Steven Clemens, B. Nagender Nath, and Warren Prell. 2016. "D18O and Salinity Variability from the Last Glacial Maximum to Recent in the Bay of Bengal and Andaman Sea." *Quaternary Science Reviews* 135(January):79–91.

Skinner, L. C. 2009. "Glacial-Interglacial Atmospheric CO2 Change: A Possible 'Standing Volume' Effect on Deep-Ocean Carbon Sequestration." *Climate of the Past* 5(3):537–50.

Stewart, A. L. and A. F. Thompson. 2015. "The Neutral Density Temporal Residual Mean Overturning Circulation." *Ocean Modelling* 90:44–56.

Stommel, Henry and A. B. Arons. 1959. "On the Abyssal Circulation of the World Ocean--I . Stationary Planetary Flow Patterns on a Sphere." *Deep Sea Research* 140–54.

Stüeken, Eva E., Michael A. Kipp, Matthew C. Koehler, and Roger Buick. 2016. "The Evolution of Earth's Biogeochemical Nitrogen Cycle." *Earth-Science Reviews*.

Sweeney, Robert E. and I. R. Kaplan. 1980. "Natural Abundances of 15N as a Source Indicator for Near-Shore Marine Sedimentary and Dissolved Nitrogen." *Marine Chemistry* 9(2):81–94.

Swinehart, D. F. 1962. "The Beer-Lambert Law." *Journal of Chemical Education* 39(7):333–35.

Talley, L. D., R. A. Feely, B. B. Sloyan, R. Wanninkhof, S. C. Doney, R. A. Fine, E. Firing, N. Gruber, D. A. Hansell, M. Ishii, G. C. Johnson, K. Katsuma, R. M. Key, M. Kramp, C. Langdon, A. M. Macdonald, J. T. Mathis, E. L. McDonagh, S. Mecking, F. J. Millero, C. W. Mordy, T. Nakano, C. L. Sabine, W. M. Smethie, J. H. Swift, T. Tanhua, A. M. Thurnherr, M. J. Warner, and J. Z. Zhang. 2015. "Changes in Ocean Heat, Carbon Content, and Ventilation: A Review of the First Decade of GO-SHIP

Global Repeat Hydrography." *Annual Review of Marine Science* 8(1):185–215.

Talley, Lynne. 2011. *Descriptive Physical Oceanography: An Introduction*.

Toggweiler, J. R. and Joellen Russell. 2008. "Ocean Circulation in a Warming Climate." *Nature* 451(7176):286–88.

Volk, T. and M. I. Hoffert. 1985. "Ocean Carbon Pumps: Analysis of Relative Strengths and Efficiencies in Ocean-driven Atmospheric CO2 Changes." *The Carbon Cycle and Atmospheric CO2: Natural Variations Archean to Present* 99–110.

Watson, Andrew and Alberto Garabato. 2006. "The Role of Southern Ocean Mixing and Upwelling in Glacial-Interglacial Atmospheric CO 2 Change." *Tellus* 73–87.

Wehrmann, Laura M., Nils Risgaard-Petersen, Heather N. Schrum, Emily A. Walsh, Youngsook Huh, Minoru Ikehara, Catherine Pierre, Steven D'Hondt, Timothy G. Ferdelman, Ana Christina Ravelo, Kozo Takahashi, and Carlos Alvarez Zarikian. 2011. "Coupled Organic and Inorganic Carbon Cycling in the Deep Subseafloor Sediment of the Northeastern Bering Sea Slope (IODP Exp. 323)." *Chemical Geology* 284(3–4):251–61.

Werner, Roland A. and Willi A. Brand. 2001. "Referencing Strategies and Techniques in Stable Isotope Ratio Analysis." *Rapid Communications in Mass Spectrometry* 15(7):501–19.

Willey, Joan D. and Arthur J. Spivack. 1997. "Dissolved Silica Concentrations and Reactions in Pore Waters from Continental Slope Sediments Offshore from Cape Hatteras, North Carolina, United States." *Marine Chemistry* 56(3–4):227–38.

Williams, Lynda B., Ray E. Ferrell, Ian Hutcheon, Allen J. Bakel, Maud M. Walsh, and H. Roy Krouse. 1995. "Nitrogen Isotope Geochemistry of Organic Matter and Minerals during Diagenesis and Hydrocarbon Migration." *Geochimica et Cosmochimica Acta*.

Wilson, M. J. 2002. "The Origin and Formation of Clay Minerals in Soils: Past, Present and Future Perspectives." *Clay Minerals* 34(01):7–25.

Woosley, Ryan J., Fen Huang, and Frank J. Millero. 2014. "Estimating Absolute Salinity (S a) in the World's Oceans Using Density and Composition." *Deep-Sea Research Part I* 93:14–20.

Worthington, L. V. and W. R. Wright. 1970. "North Atlantic Ocean Atlas of Potential Temperature and Salinity in the Deep Water Including Temperature, Salinity and Oxygen Profiles from the Erika Dan Cruise of 1962." *Tellus*.

Wunsch, Carl. 2016. "Pore Fluids and the LGM Ocean Salinity - Reconsidered." *Quaternary Science Reviews* 135:154–70.

Yang, Kiho, Jin Wook Kim, Toshihiro Kogure, Hailiang Dong, Hionsuck Baik, Bryce Hoppie, and Robert Harris. 2016. "Smectite, Illite, and Early Diagenesis in South Pacific Gyre Subseafloor Sediment." *Applied Clay Science* 134:34–43.

Yokoyama, Yusuke, Kurt Lambeck, Patrick De Deckker, Paul Johnston, and L. Keith Fifield. 2000. "Timing of the Last Glacial Maximum from Observed Sea-Level Minima." *Nature* 406(6797):713–16.

Zerkle, A. L. and S. Mikhail. 2017. "The Geobiological Nitrogen Cycle: From Microbes to the Mantle." *Geobiology*.

Zhang, Lin, Mark A. Altabet, Taixing Wu, and Ora Hadas. 2007. "Sensitive

Measurement of NH4+ 15N/14N (Δ15NH4+) at Natural Abundance Levels in Fresh and Saltwaters." *Analytical Chemistry* 79:5297–5303.

Zhang, Xinning, Daniel M. Sigman, François M. M. Morel, and Anne M. L. Kraepiel. 2014. "Nitrogen Isotope Fractionation by Alternative Nitrogenases and Past Ocean Anoxia." *Proceedings of the National Academy of Sciences* 111(13):4782–87.